Faculté des bioingénieurs

Integrating Existing High Resolution Geospatial Datasets for LoD2 Building Modelling

Accuracy Evaluation and Comparative Analysis in Louvain-la-Neuve

Author: Kailu Chen

Supervisors: Pierre Defourny & Raivo Aunap

Jurors: Julien Radoux & Erika Lepers

Academic year: 2024-2025

Submitted in partial fulfillment of the requirements for the degree of: Master [120] in agricultural sciences and bio-industries, with a professional focus: GEM – Geo Information Science and Earth Observation for Environmental Modeling and Management (SAIV2MS/GM)

Acknowledgements

First and foremost, I would like to express my sincere gratitude to the GEM (Geo-information Science and Earth Observation for Environmental Modelling and Management) programme for granting me the opportunity to embark on this unique and enriching academic journey across different cultures and institutions. This experience has profoundly shaped both my academic growth and personal development.

I would especially like to thank Prof. Pierre Defourny, my supervisor, for proposing this inspiring research topic and for his continuous guidance throughout the project. His constructive feedback and encouragement have been instrumental to my progress. My heartfelt thanks also go to Prof. Raivo Aunap, my second supervisor, for his generous support, insightful advice, and patient mentorship, which greatly helped me in overcoming challenges during the research process.

I am also grateful to Dr. Julien Radoux for his valuable assistance with data acquisition, which was essential to the implementation of this study.

Beyond academia, I would like to extend my deepest appreciation to the friends who stood by my side, offering support and companionship during this demanding journey—Ruoxi, Vian, Sena, Zhou—your presence has been a source of strength and motivation. Thank you for believing in me.

Last but by no means least, I owe my deepest thanks to my family—my sister Kaiwen, and especially my parents—for their unwavering love, patience, and belief in me. You have always been my greatest source of support, and I am endlessly grateful. I love you all.

Abstract

Accurate representation of the built environment is essential for urban planning, analysis, and decision-making. This thesis focuses on constructing a detailed 3D building model of Louvain-la-Neuve by integrating multiple high-resolution spatial datasets. Specifically, the study assesses the compatibility between LiDAR and PICC building footprints, and examines how each dataset contributes to the generation of Level of Detail 2 (LoD2) building models.

To achieve this, building footprints from both datasets were compared in terms of geometric alignment, shape similarity, and attribute completeness. The study also evaluated how differences in data resolution and classification quality influence the modeling process. A semi-automated 3D building modeling workflow was implemented using rule-based methods, and the resulting model was assessed for geometric accuracy against a LiDAR-derived digital surface model (DSM).

The findings reveal notable differences in footprint precision and roof segmentation accuracy between the datasets. While LiDAR provides more detailed elevation data, PICC offers consistent and cartographically clean building outlines. Their integration improves the overall completeness of the model but introduces challenges in data fusion and height assignment.

This research highlights the importance of understanding dataset interoperability when generating LoD2 building models and offers practical insights into the contributions and limitations of different data sources. The results aim to support future applications in urban analysis and sustainable city planning for Louvain-la-Neuve.

Key words: 3D building model; LoD2; LiDAR; PICC; Orthophoto; dataset compatibility; footprint comparison; data fusion

Table of Contents

List of Figures

List of Tables

List of Acronyms

3DCM	3D city model
LoD	Level of Detail
DTM	Digital Terrain Model
DOM	Digital Orthophoto Map
DEM	Digital Elevation Model
OSM	OpenStreetMap
ALS	Airborne Laser Scanning
TLS	Terrestrial Laser Scanning
MLS	Mobile Laser Scanning
UAV	Unmanned Aerial Vehicles
DSM	Digital Surface Model
nDSM	normalized Digital Surface Model
3D GIS	3D Geographic Information Systems
AEC	Architecture, Engineering, Construction
FM	Facilities Management
RANSAC	Random Sample Consensus
PICC	Projet Informatique de Cartographie Continue
RMSE	Root Mean Square Error

Chapter 1. Introduction

With ongoing urbanisation and continuous population growth, addressing urban challenges in a more comprehensive, efficient, and intuitive way has become a major task (Shahidehpour et al., 2018). Given the increasing complexity of urban environments and issues, traditional 2D models are no longer sufficient to meet modern planning and management demands. In response, emerging concepts such as smart cities and digital twins have been introduced to offer high-precision and comprehensive digital representations of the physical world (Silva et al., 2018). At the core of these frameworks lies the 3D city model (3DCM), which plays a critical role in supporting urban planning, development, and policy-making (Dimitrov & Petrova-Antonova, 2021).

3D city models are typically characterised by different levels of detail (LoD), as defined in the CityGML standard, ranging from LoD 0 to LoD 4. As the LoD increases, the semantic richness and geometric complexity of the represented objects also grow. LoD0 represents basic 2.5D digital terrain models (DTMs) with building footprints or roof edge polygons. LoD1 adds building height information to create simple block models, typically with flat roofs. LoD2 introduces differentiated roof structures based on the LoD1 geometry. LoD3 includes more detailed architectural elements such as windows and doors, while LoD4 provides indoor modelling, including internal walls, staircases, and rooms. Although higher LoDs enable more advanced applications, they also require markedly more data and computational resources.

Various types of data and methods exist for constructing 3D city models to meet the diverse needs of different application domains. Common data sources include 2D topographic maps—often from governmental or open datasets—LiDAR point clouds, and aerial or satellite imagery. The growing availability of high-resolution spatial datasets has created new opportunities for 3D modelling but also presents new challenges. Each dataset has its strengths and limitations; relying on a single source often leads to trade-offs between local geometric accuracy, model completeness, and spatial coverage. Therefore, integrating multiple data sources is essential for fully leveraging the potential of 3D city models and improving their accuracy.

Despite the advancements in data acquisition technologies, integrating multi-source datasets for accurate 3D city modelling remains a complex task. Challenges include inconsistencies in spatial resolution, data formats, temporal differences, and semantic interpretation across datasets. Moreover, automated tools for modelling often operate as black boxes, limiting the user's control over critical decisions such as roof type recognition or segmentation precision. These issues are particularly relevant when aiming for LoD2-level models, where detailed roof geometry plays a significant role in the model's overall fidelity.

This study addresses the following core question: How can high-resolution datasets such as LiDAR point clouds, official building footprints, and orthophotos be effectively integrated to construct accurate LoD2 building models? The compatibility between these datasets is also investigated, and the reliability of semi-automated modelling tools is evaluated the reliability in practical scenarios.

The primary objective of this study is to develop a LoD2-level 3D city model using three high-resolution spatial datasets: classified LiDAR point clouds, building footprint data from the PICC database, and an orthophotography image. The modelling process is carried out using the *3D Buildings* solution provided by ArcGIS, a semi-automated tool designed to streamline building reconstruction from LiDAR data. Through this approach, we aim to assess how each dataset contributes to model quality and how its combined use enhances overall performance.

This study contributes to the broader field of 3D urban modelling by demonstrating how multiple data sources can be jointly leveraged to produce more accurate and reliable LoD2 models. Exploring the advantages and limitations of each dataset offers practical insights into selecting and combining data for different modelling purposes.

Furthermore, the findings provide a solid foundation for future applications such as solar potential analysis, urban risk assessment, and smart city planning. By evaluating the performance of semi-automated tools and identifying key sources of error, this research also offers valuable guidance for improving modelling workflows and ensuring scalability across different urban environments.

Chapter 2. Literature Review

This chapter will introduce the current research status through a literature review of 3D city models, modelling methods, data fusion, and the application of 3D city models for urban problem analysis.

2.1 3D City Model

2.1.1 Definition

3D city models (3DCMs) could play an increasingly important role in urban planning and management. It serves as a presentation of the urban setting through three-dimensional geometric forms of typical urban objects and structures, among which buildings stand out as the most significant feature (Biljecki et al., 2015). The objects of concern in urban areas typically encompass buildings, transportation networks, vegetation, waterways, and public facilities. Based on the geometric elements of the 3D city model for division, its hierarchical structure can be classified as 2D Digital Orthophoto Map (DOM), 2.5D DEM (Digital Representation of the Surface Terrain), 2.5D Linear Elements (such as roads, rivers, boundaries of land use, etc., representing the contours of objects) and 3D Solid Objects (such as buildings, bridges, pipelines, etc., representing the entire volume of objects) (Zhu et al., 2009). Within these features, 3DCMs can overcome the limitations of traditional 2D representations (Lafioune & St-Jacques, 2020), providing realistic information about buildings, vegetation, topography, and other features within the city. In addition to geometric and graphical features, semantic features are also a crucial component of 3DCM. It means that 3DCM can also contain the logic and spatial interrelationships between different objects. For example, all objects belong to a group of predefined classes with spatial and thematic attributes, such as Buildings, Roads, City Furniture or Water Bodies, etc. Complex objects can be further decomposed. For instance, buildings can be divided into roofs, walls, floors, etc., and walls can be decomposed into windows and doors. These features play a key role in urban data integration, associating data from different fields with the corresponding urban objects (Kolbe & Donaubauer, 2021), thus enabling the observation and understanding of both the current state of urban development and future plans (Lee et al., 2020).

2.1.2 Applications for 3D City Models

At present, 3DCM has been applied in a large number of fields for different analytical purposes (Biljecki et al., 2015). For example, in the aspect of energy management, 3DCMs facilitate the management of utilities and natural resources, such as water and energy (Boates et al., 2018). Besides, estimating the solar radiation potential on the surface of buildings is a main use case for applying 3D city models (Fath et al., 2015; Redweik et al., 2013); the estimation of household energy demand is also a use case that can demonstrate the value of semantic 3D city models (Agugiaro, 2016; Bahu et al., 2013). There are also some typical applications, such as cadastre (Stoter et al., 2013) and routing (Hildebrandt & Timm, 2014). Also, in urban planning, 3D city models can provide such as visibility analysis (Delikostidis et al., 2013), shadow analysis (Hwang et al., 2011; Lafioune & St-Jacques, 2020), traffic noise analysis (Lu et al., 2017), urban skyline analysis (Czyńska & Rubinowicz, 2014), etc. Furthermore, 3D city models can also be used in disaster management and emergency response (Tashakkori et al., 2015) to predict the risks and potential damages of disasters such as earthquakes (Kemec et al., 2010), floods (Varduhn et al., 2015), etc.

Figure 1. 3D city model applications

(source: Biljecki et al., 2015)

Nowadays, many cities around the world have built their city models to address different urban challenges. For example, Hong Kong has created an interactive 3D noise visualisation model to reduce road traffic noise (Law et al., 2011), while the city of Chennai in India has created a

3D city model to measure the impact of rapid urbanisation on existing infrastructure, supporting better planning (Ahmed & Sekar, 2015).

2.2 Data Sources and Modelling Methods

2.2.1 Types of Data Sources

Over the past few decades, the construction and development of 3D models have accelerated markedly (Yan et al., 2019). However, obtaining large-scale and high-resolution 3D models is still challenging due to the complexity of urban scenes and the limitations of existing methods. Currently, the data for generating 3D city models mainly include:

(1) 2D topographic maps, i.e., GIS data describing urban objects containing geometry, land use and other attributes (Shiode, 2000). This type of data is mainly sourced from government agencies, and in recent years, open-access geographic datasets such as OpenStreetMap (OSM) have emerged. However, their accuracy and completeness need to be confirmed (Chen et al., 2018). Nowadays, some countries and governments have also published geospatial data as open data sources on their websites to meet public and private needs (Zhu et al., 2015).

(2) LiDAR point cloud data, which is generated through the utilisation of a laser projected onto a surface, then captured and reflected to generate a three-dimensional point cloud (Chen et al., 2018). Depending on the specific implementation of the technique in different application scenarios and different acquisition methods, it can also be divided into the following categories: airborne laser scanning (ALS) data (Jovanović et al., 2020; Verma et al., 2006), terrestrial laser scanning (TLS) data (Fruh & Zakhor, 2001), and mobile laser scanning (MLS) data (Liu et al., 2020). The use of lidar point clouds meets the need for large-scale, high-quality data input, but also faces challenges of accuracy and geometric detail. For example, for segmentation of building instances, due to the large number of cluttered objects in an urban scene, identifying and separating individual buildings from a massive point cloud becomes a serious challenge; data incompleteness, although there are multiple methods for lidar acquisition, data originating from only one method is usually used, and this back to the limitations of acquisition due to the fact that single acquisition methods have their limitations on positioning and movement trajectories, e.g., airborne lidar

may not be able to capture the vertical walls of a building; Moreover, the difficulty of obtaining topologically accurate surface models is further compounded by the architectural complexity of real-world buildings and the limited structural information that can be derived from sparse and noisy point clouds (Huang et al., 2022). Another limitation is that its generated models contain only geometric data without semantic information, which has to be further supplemented with data if needed (Gimenez et al., 2015).

(3) Aerial imagery, or satellite imagery, is a typical data source for constructing large-scale 3D models that can provide high-resolution images, which are captured by flying vehicles (aircraft, drones, satellites). The use of aerial imagery (Abdul & Sadeq, 2024; Adreani et al., 2022) to reconstruct entire urban scenes is becoming more prevalent due to the pervasive deployment of unmanned aerial vehicles (UAVs) (Chen et al., 2018; Xie et al., 2012). Where image quality is critical, weather and flight conditions can have an impact on image quality, such as creating occlusions. The method used to generate buildings is to extract building contours from a digital surface model (DSM) obtained from aerial imagery (Gimenez et al., 2015).

However, 3D models constructed from a single data source often have limitations and cannot simultaneously take into account the local accuracy, overall integrity, and scope of the scene. The fusion of multiple data sources can aggregate the advantages of each source and add richer perceptions, perspectives, and dimensions to the generated models (Liu et al., 2023). Therefore, the fusion of multiple data sources has attracted more and more attention (Wang et al., 2022). For example, point cloud data obtained from 3D laser scanning will inevitably suffer from aperture distortion and tilt problems after registration. Secondary measurements are also affected by the cost, which makes the results unsatisfactory. Wang et al. (2022) carried out a study on the fusion of 3D laser point cloud models and UAV images, and obtained high alignment integrity, which compensated for the lack of ground-based 3D laser acquisition at the top and the lack of UAV detail at the bottom of the building. However, the study was limited to modelling buildings and did not address other aspects, such as roads. Wen et al. (2019), on the other hand, established a 3D road boundary recovery framework by using, among others, MLS point clouds, spatial trajectory data, and remote sensing imagery, which effectively solved the problem of missing road boundaries and successfully recovered them.

As these data sets typically prioritise disparate objectives, encompass distinct dimensions, or focus on a singular entity, such as a building or terrain, and encompass disparate data types, the challenge of data heterogeneity is frequently encountered when integrating these data sets (Gröger & Plümer, 2012). Consequently, the ability to integrate disparate data in a manner that facilitates seamless integration and minimises errors represents a crucial aspect of the process of developing 3D models.

2.2.2 Level of Detail (LoD)

Level of Detail (LoD) is a key concept in 3D city modelling, describing the geometric complexity and semantic richness of urban objects at various scales. The concept was first formalised in the CityGML standard, which remains one of the most widely used schemas for representing and exchanging 3D city models (Ying et al., 2023). One of its main contributions is the definition of a structured LoD hierarchy, which has been widely adopted even beyond the CityGML format.

CityGML defines five LoD levels, progressively incorporating more detailed geometrical and semantic information. As the LoD increases, the semantic richness of the objects concomitantly escalates(Gröger & Plümer, 2012). LoD0 represents a digital terrain model, essentially a 2.5D elevation model of the building footprint. LoD1 consists of basic box-shaped building models representing buildings in their simplest form, with flat roofs and no detailed features. LoD2 extends LoD1 to incorporate roof structures. At this detail level, external details of the buildings and plants are displayed at a certain scale. LoD3 provides detailed building models with openings (e.g., windows, doors) and optional textures, while LoD4 includes internal structures such as internal rooms, interior doors, stairs, and furniture within the building (Buyuksalih et al., 2019; Karim et al., 2022).

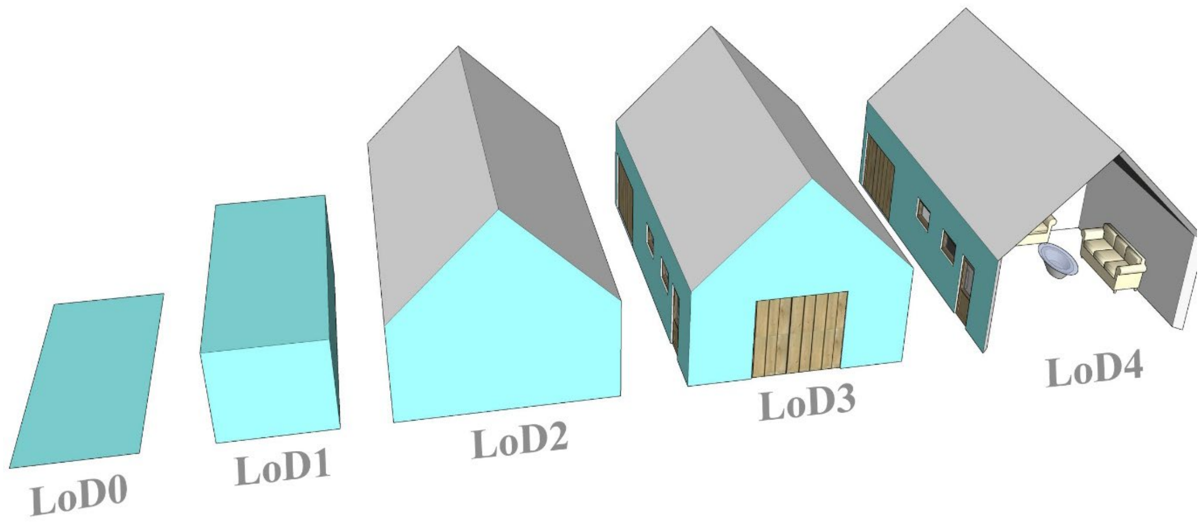

Figure 2 Five Level of Detail (LoD) provided by CityGML

Usually, most applications related to 3D building modelling are not satisfied with a simple LoD1 model but want the model to have at least a roof shape (LoD2 or higher). This dynamic visualisation of LoD helps it to be applied to different domains, e.g. low-level LoD can extract large-scale object information, while high-level LoD can focus on more subtle 3D objects (Ying et al., 2023). Among these, LoD2 is particularly relevant for many urban applications. It offers a good balance between geometric realism and modelling effort, making it widely used in studies related to solar radiation, energy simulation, and roof-based analyses. In our study, LoD2 was selected as the target level for building model development, focusing on the representation of roof forms and building volumes using high-resolution multi-source datasets.

Several practical implementations of LoD-based models have been demonstrated in urban environments. For instance, in the city of Helsinki, the LoD3 city model has been implemented and made public (virtualcitySYSTEMS, 2017). A LoD2 country model was made across Estonia (*Maa-Amet 3D*, n.d.). Eleven cities in France have also introduced city models with accuracies reaching LoD1-2 (Lafioune & St-Jacques, 2020). Bolte et al. (2024) used a DTM, a CityGML-based LoD2 semantic 3D city model, lidar data and 2D land use data from the German Official Property Cadastral Information System (ALKIS) for 3D urban environment modelling to calculate green windows view index (GWVI). These examples highlight the flexibility of LoD-based modelling across different geographic scales and tools, regardless of whether CityGML is used as the actual exchange format.

2.2.3 Digital Elevation Models

Digital elevation models (DEMs) provide a fundamental representation of the Earth's surface in three dimensions and have been widely applied across multiple disciplines (Guth et al., 2021). In the context of 3D building modelling, DEMs and their derived products are often integrated with other data sources to support various modelling tasks. In this study, three types of elevation-related datasets were employed: Digital Terrain Model (DTM), Digital Surface Model (DSM), and normalised Digital Surface Model (nDSM).

A Digital Elevation Model (DEM), in its strictest sense, refers to a "bare-earth" elevation surface, ideally excluding vegetation, buildings, and other above-ground features.

A Digital Surface Model (DSM), by contrast, captures the elevations of the highest surfaces at each location, including rooftops, treetops, and bare ground where no vertical structures are present.

A Digital Terrain Model (DTM) is a broader term that encompasses digital representations of the ground surface, potentially including additional terrain characteristics such as landforms, drainage patterns, and soil properties. When the model focuses exclusively on elevation values, it essentially functions as a DEM, making the DEM a subset of the DTM (Zhou, 2017).

Figure 3 Digital Surface Model (DSM) and Digital Terrain Model (DTM)

Source: Adapted by the author from Guth et al., (2021)

The normalized Digital Surface Model (nDSM) represents the absolute height of man-made or natural features relative to the ground (S.A.M.HASHEMI, 2008). It is calculated by subtracting the DTM from the DSM at each corresponding location:

$$nDSM = DSM - DTM \quad (1)$$

These elevation models are essential for extracting building heights, analysing roof forms, and supporting accurate 3D reconstruction in urban environments.

2.2.4 Building Reconstruction Methods

Approaches to creating 3D city models are diverse (Ying et al., 2023), with different domains having different focuses, such as 3D Geographic Information Systems (3D GIS), computer graphics, and Architecture, Engineering, Construction and Facilities Management (AEC/FM), where different modelling paradigms are used. In 3D GIS, the modelling focuses on the management of multi-scale, large-area and geo-referenced 3D models, while the AEC/FM domain addresses more detailed 3D models related to construction and management processes, and computer graphics concentrates rather on the visual appearance of 3D models (Zhu et al., 2009). Methods of creating 3D city models are varied. One of the methods related to building reconstruction can be divided into three categories: data-driven, model-driven, and a combination of data-driven and model-driven.

Model-driven methods make a prior choice between primitive and complex buildings. Thus, for a point cloud obtained on a primitive building, the method consists of searching for the most suitable model among the basic building shapes contained in the model library. The most probable parameter values are then calculated and assigned to the parameters of the selected model. The method requires first extracting the original building, a simple building that can be described by a set of parameters calculated before constructing the 3D model. The next step would be to determine the roof details of the building and then construct the building model. In summary, there are two types of parameters used to describe a building in a model-driven approach: one that defines the polygons of the building ground (location of the building footprint, orientation, etc.) and one that describes the building space (spatial parameters, which define the building roof plane).

The data-driven approach does not consider the form of the building in advance. It will only use the input data as initial data, so this approach can generate models without specifying a specific library for each building. It analyses the building point cloud as a unity without having to associate it with a set of parameters. The modelling consists of two stages: roof modelling and façade modelling. For roof modelling, there have been many different approaches, such as the RANSAC (Random Sample Consensus) technique, 3D Hough-Transform and algorithms for area growth. For elevation modelling, two approaches exist, one before and the other after segmenting the roof plane.

Both approaches have advantages and disadvantages. The model-driven approach is able to consider the entire dataset and can quickly provide geometric models without visual deformation. Since there are pre-defined parametric shapes, when some building roof data is missing (due to reflections or obstacles), it is still possible to construct complete building roofs from the predefined shapes, but it may fail for some complex buildings or for building types for which the predefinitions do not exist. The data-driven approach is more flexible and tends to simulate each part of the building to obtain the closest or most reliable polyhedral model (if the point cloud is homogeneous and its density is related to the dimension of the elements to be extracted, the model obtained will be very faithful to the original building), however, it is also more prone to visual deformations and requires a longer processing time. The data-driven approach is also the only one capable of dealing with the general case of unspecified form buildings, although there may be a risk of obtaining distorted models (Tarsha-Kurdi et al., n.d.).

The hybrid-driven approach combines both data-driven and model-driven methods. Typically, it uses the data-driven approach to extract the planar primitives of buildings and construct a roof topology graph to store topological relationships, while employing the model-driven method to search and fit point clouds in the topological space. For the reconstruction of large-scale complex scenes, this modelling method can be adopted, applying the model-driven approach in areas with regular building structures and the data-driven approach in areas with irregular building structures (Wang et al., 2023).

2.3 Challenges in LoD2 Modelling

Although extensive research has been conducted on 3D building reconstruction and significant progress has been made regarding LoDs, several challenges remain at the LoD2 level (Wang et al., 2023). These include efficiently identifying building structures and accurately segmenting building surfaces (Verdie et al., 2015). Özdemir et al. (2021) further highlight the complexity of the workflow involved when relying on a single data source, particularly in tasks such as scene classification and object recognition. Inaccurate segmentation results—such as over-segmentation or under-segmentation—can lead to unpredictable errors during the subsequent reconstruction of building surface topology.

Chapter 3. Research objectives

With the growing demand for accurate and detailed urban analysis, traditional 2D GIS approaches have become insufficient for capturing the spatial complexity of urban environments—particularly in areas with heterogeneous building forms and high-density development. In response, 3D representation of urban features has gained momentum, offering new opportunities for visualisation, measurement, and spatial reasoning. However, building a reliable 3D representation requires more than just advanced modelling tools—it hinges on the quality, consistency, and compatibility of the input datasets.

This thesis focuses on constructing a building-level 3D model for the city of Louvain-la-Neuve using multiple high-resolution spatial datasets, including LiDAR point clouds, cadastral building footprints from Projet Informatique de Cartographie Continue (PICC), and orthophotos. The model targets the LoD2 level, which includes building footprints with roof form information. Rather than attempting to create a comprehensive 3D city model, the research concentrates on buildings only, using LoD2 as the target level of detail due to its balance between geometric expressiveness and data availability.

A key aspect of this study lies in understanding how different datasets—each with its spatial resolution, geometric characteristics, and acquisition methods—can be aligned, merged, or compared to support accurate and consistent 3D building modelling. Specifically, the thesis explores two major dimensions: the geometric compatibility between LiDAR-derived and PICC building footprints, and the contribution each dataset makes to the resulting 3D model's accuracy and completeness. These investigations aim to provide methodological insights into dataset integration for urban modelling, while also highlighting practical limitations in using commonly available spatial data.

Based on these objectives, the research is guided by the following questions:

To what extent are the LiDAR and PICC building footprints geometrically compatible, and how do their differences affect the integration process for constructing LoD2-level 3D building models?

What are the respective contributions of LiDAR data, PICC footprints, and orthophotos to the accuracy, completeness, and structural realism of the resulting 3D building models?

Chapter 4. Materials

4.1 Study Area

The study area for this research is Louvain-la-Neuve, located in the Walloon Region of Belgium, approximately 30 kilometres south of Brussels, within the municipality of Ottignies (Fig. 4).

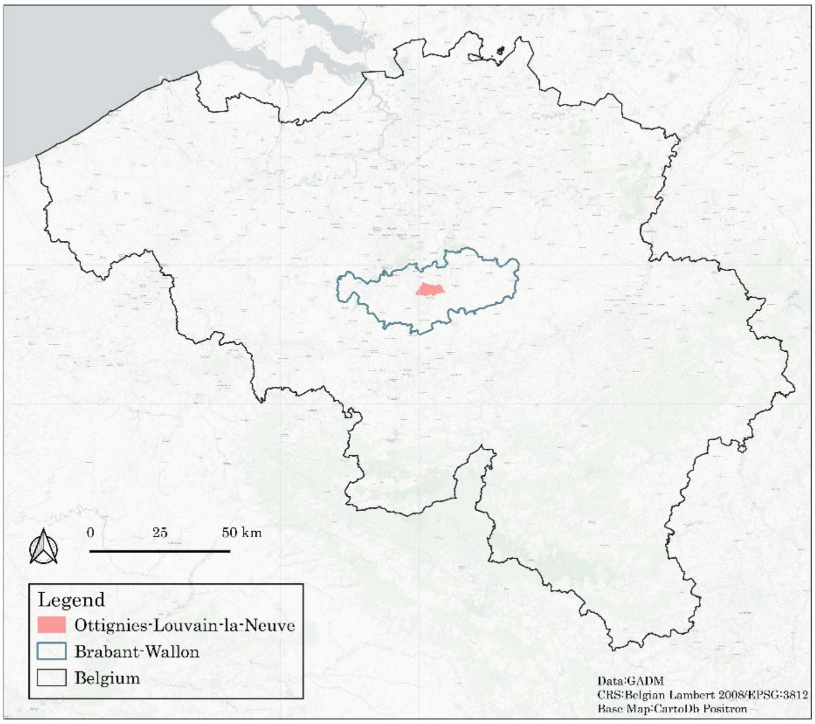

Figure 4 Location of Louvain-la-Neuve

Established in 1972, the city was purpose-built in response to a major linguistic conflict in the 1960s. At that time, Flemish nationalists had long called for the removal of the French-speaking section of the Catholic University of Leuven, which was situated in the Dutch-speaking part of the country. The conflict escalated markedly, with Flemish nationalist students regularly marching through the city, chanting slogans hostile to French speakers, including the notorious "Walen buiten" ("Walloons out") ("Affaire de Louvain," 2025). This political crisis eventually resulted in the split of the Catholic University of Leuven into two separate institutions: the Dutch-speaking Katholieke Universiteit te Leuven (KUL), which remained in Leuven, and the French-speaking Université catholique de Louvain (UCL), which relocated to the Walloon Region.

The new site for the French-speaking university was selected in the municipality of Ottignies, on a vast hilly plateau at the edge of the Lauzelle Forest. At the time, the area was largely rural, consisting of farmland, marshes, and only a few scattered farms and dwellings in the village of La Baraque ("Louvain-la-Neuve," 2025). As a purpose-built university town, Louvain-la-Neuve was designed with a strong focus on pedestrian-friendly urban planning. One of its defining characteristics is the separation of pedestrian and vehicular traffic: most car traffic is directed underground, while the city centre and many neighbourhoods are car-free, prioritising pedestrians and cyclists (VISITWallonia, n.d.). Today, Louvain-la-Neuve is a rapidly growing city offering a wide range of functions—not only academic, but also residential, commercial, and cultural. It features shopping centres, cinemas, conference halls, museums, and other amenities that serve both students and permanent residents (https://www.olloweb.com, 2024). Architecturally, the city adheres to specific guidelines such as low-rise buildings, the using of brick façades, numerous covered walkways, and a diversity of distinct architectural styles (*Une ville nouvelle*, n.d.).

Figure 5 The selected study area for detailed analysis

This study area was selected due to the availability of high-resolution LiDAR point cloud data, official vector datasets, and orthophotos. In addition, the complexity and variation in local building types add both challenge and value to the study. However, given the high volume of data and the computational demands of processing it, only a representative section of Louvain-la-Neuve was eventually selected for detailed analysis (Fig. 5).

4.2 Lidar Point Cloud

The LiDAR point cloud data used in this study were provided by the Walloon Public Service (SPW ARNE & SPW Digital, 2024) and cover the entire Walloon Region (17000km^2). Data acquisition was carried out by Sintegra, the company awarded the contract for this project. The data were collected during two winter campaigns: from 6 December 2020 to 1 April 2021, and from 14 January 2022 to 5 March 2022, with a total flight duration of approximately 120 hours. The main objective of this survey was to update and improve the precision of the earlier LiDAR dataset acquired in 2013–2014 (Table 1).

Table 1 Comparison between Lidar from 2013-2014 and from 2021-2022

source: (*LiDAR 2021-2022 | Géoportail de La Wallonie*, n.d.)

	Lidar 2013-2014	Lidar 2021-2022
Number of Pulses/m^2	1.5	7
Z-precision	12cm	12cm
XY projection system	Lambert 72	Lambert 2008
Z projection system	DNG*	DNG
Overlap between two flight strips	30%	60%

**DNG: Datum de Nivellement Général – the Belgian national vertical datum used for orthometric height.*

The dataset was acquired through airborne laser scanning. A LiDAR sensor mounted on an aircraft emitted laser pulses toward the ground and measured the return time of each pulse via backscattering. The flight followed a predefined plan consisting of multiple parallel flight paths, with an average pulse density of 7 points per square metre. The general information used for the flight is shown in Table 2.

Table 2 LiDAR Data Acquisition Flight Parameters

Source: (MÉCHIN, 2023)

Time on site	120h30
Average aircraft speed (kts)	170

Average flight height AGL (m)	2400
Type of LiDAR used	Double LMSQ780 and Double VQ780II-S
LIDAR acquisition frequency (kHz)	900
Minimum emission pulse density required (PTS/m^2)	> 1.5 pulse ground sol / m²
Pulse emission density per band (pulse/m^2)	6.8 pulse/m²

The final deliverables were provided in the Belgian Lambert 2008 coordinate reference system (ETRS89 / Belgian Lambert 2008). The classification system used for the point cloud is detailed in Table 3.

Table 3 Classification of Lidar products

source: Utilisation des produits LiDAR, Rédaction : SPW ARNE et SPW Digital – Mai 2024

Code	Description
Class 0	Unclassified
Class 1	Above-ground (buildings, roofs and others)
Class 2	Ground (including embankment and dikes)
Class 4	High vegetation (including linear vegetation)
Class 9	Water
Class 10	Bridge
Class 15	High voltage lines

The average point spacing is approximately 0.26 metres. Each LiDAR point contains several attributes (Fig. 6), including:

Elevation: Altitude of the point relative to the DNG

Class Code: The type of object that reflected the pulse (e.g., ground, vegetation, building).

Return Number: Indicates the return order for each pulse (up to five returns possible).

Intensity: Varies depending on surface reflectance (albedo), driven by material, moisture, and sensor characteristics.

GPS Time: The GPS timestamp of when the pulse was emitted.

Scan Angle Rank: Angle of the laser pulse relative to nadir, expressed between –90° and +90°. A value of 0° corresponds to nadir (directly beneath the aircraft); –90° indicates the left side, and +90° the right side, relative to the flight direction. Most current LiDAR systems operate within ±30° (source: Esri).

Scan Direction Flag: Indicates the movement direction of the scanning mirror. A value of 1 represents a positive scan direction (left to right along the flight path), while 0 indicates a negative direction (source: Esri).

LAS File	LIDAR_2021_2022_500mN6505E6675_1.las
Location	D:\coursework\THEISI\working\data
Elevation	140.66 m
Coordinates	4.6190110°E 50.6685500°N
Class Code	6
Return	1 of 1
Classification Flag(s)	None
Intensity	687
User Data	0
Point source ID	40046
Point Record	779098
GPS time	1328775485.431 standard time
Scan angle rank	-3
Scan direction flag	0
Edge of flight line	0

Figure 6 Information available forced in terms of attributes in ArcGIS Pro

The full LiDAR dataset for the Walloon Region comprises 69,438 individual tiles, each covering an area of 500 × 500 metres. For this study, only a single representative tile—located at coordinates N6505E6675—was selected for analysis.

4.3 Projet Informatique de Cartographie Continue (PICC)

The PICC (Projet Informatique de Cartographie Continue) is a 3D digital cartographic reference for the Walloon Region. It inventories all identifiable elements of the landscape using precise x, y, z coordinates, with a spatial accuracy of less than 25 cm. The dataset includes a wide range of features (*Projet Informatique de Cartographie Continue (PICC) | Géoportail de La Wallonie*, n.d.), such as:

- Built structures: buildings and engineering constructions;
- Infrastructure elements: equipment such as plywood, columns, pylons;
- Transport networks: railway and road networks, including main roads, footpaths, and green belts;
- Hydrological features: rivers and streams;
- Land use elements: isolated trees, sports fields, parcel boundaries;
- Geomorphological features, such as dykes.

The PICC is compiled from various data sources, including:

- 3D vector maps produced by private companies based on stereo digital photography;
- Topographic surveys commissioned through public contracts;
- Vector maps generated by the Geometrology Department of SPW (Service Public de Wallonie) based on topographic surveys;
- 3D surveys submitted to SPW by contractors under the WALTOPO agreement.

All datasets, regardless of origin, are systematically verified, tested, and validated by SPW before inclusion in the PICC.

Two versions of the PICC are available. The first one is a public version – freely accessible to all users, offering general cartographic data. Another one is a restricted version – available exclusively to WALTOPO-affiliated companies, containing more detailed information, such as types of equipment, curbs, and tree species. Both versions are regularly updated to ensure the information remains current (*PICC : La Référence Cartographique de La Wallonie | Géoportail de La Wallonie*, n.d.).

In this study, the PICC was used primarily for extracting building roof borders and building footprint data. Similar to the LiDAR dataset, only a clipped portion of the dataset covering the study area was selected for analysis.

4.4 Orthophoto

The orthophoto used in this study is a GeoTIFF image with a spatial resolution of 4 cm per pixel, acquired in 2022(Fig. 7). It was acquired by the Geomatics Research Laboratory of Université catholique de Louvain (UCLouvain) for scientific purposes. The image covers a large area, with dimensions of 131,633 pixels by 124,377 pixels. The dataset is projected in the ETRS89 / Belgian Lambert 2008 coordinate reference system (EPSG:3812). The pixel size corresponds to 0.04 meters (4 cm) in both the X and Y directions. This orthophoto contains four bands: red, green, blue, and an alpha transparency band. JPEG compression was applied, ensuring minimal loss of image quality.

In this study, the image primarily serves as an accurate planar reference for validation purposes.

Figure 7 Orthophoto of study area in Louvain-la-Neuve, 2022 (ELI, 2022)

Chapter 5. Methods

This chapter provides a detailed explanation of the complete methodology adopted in this research. The main tools used in this study are ArcGIS Pro and the 3D Buildings solution from ArcGIS.

5.1 Workflow Chart

Figure 8 presents the overall workflow of this study. LiDAR point clouds and PICC datasets were used to generate and validate a LoD2 building model. The process includes selecting a study tile, extracting elevation models and building footprints, segmenting roofs, and generating a 3D model. RMSE analysis was performed to assess accuracy, followed by manual adjustments. The final model was validated both vertically (using PICC eave heights) and horizontally (using PICC footprints and orthophotos).

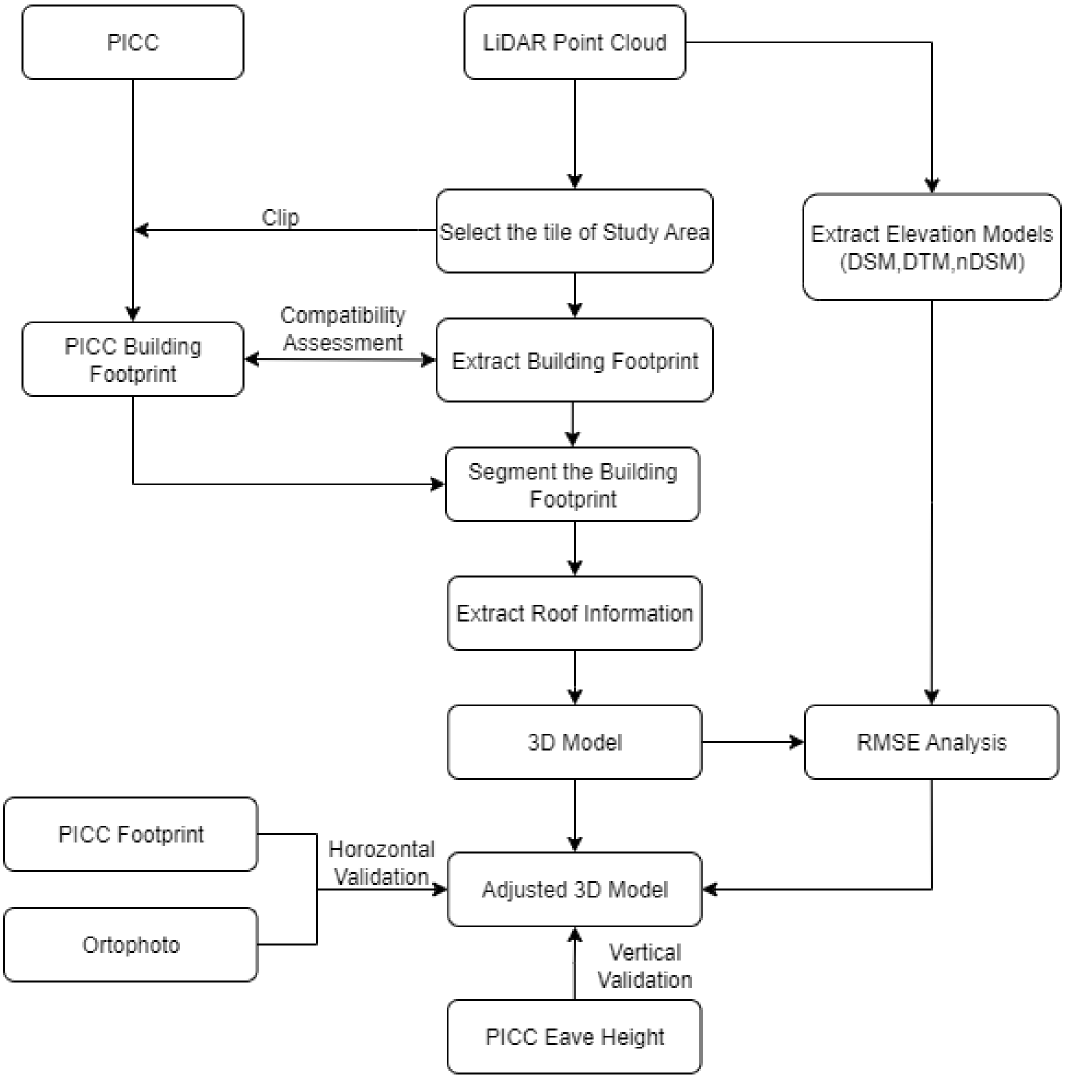

Figure 8 Workflow for LoD2 Building Model Generation and Validation

5.2 Modelling Urban Buildings at LoD2 Level

5.2.1 Extracting Elevation Models from LiDAR Point Clouds

To derive elevation information for the study area from the LiDAR point cloud data, three key surface models were first generated: the Digital Surface Model (DSM), Digital Terrain Model (DTM), and normalised Digital Surface Model (nDSM). The DTM serves as the terrain base in the 3D scene, while the DSM and nDSM provide elevation data necessary for building reconstruction.

Accurate classification of the point cloud is essential for generating reliable elevation models. In this study, the point cloud dataset had already been classified (Table 3), and therefore, no additional classification process was conducted initially. However, during the subsequent modelling process, it was observed that certain roof points were not correctly classified under the 'building' category. This misclassification led to significant inaccuracies in some extracted building footprints. To address this issue, a manual adjustment was made: point clouds that were evidently part of building rooftops but were not labelled as such were reclassified into the 'building' category (Fig 9).

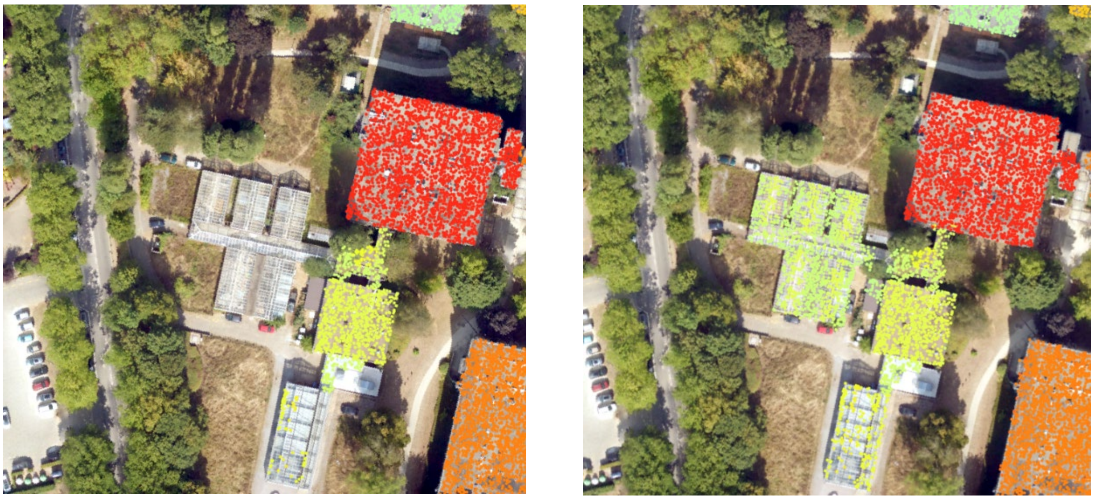

Figure 9 left: Building point cloud before manual adjustment; right: Building point cloud after manual adjustment

When generating the DTM—which represents bare-earth elevation—only points classified as 'ground' were selected. In contrast, the DSM was created without any filtering, to capture the elevation of all surface features. Finally, the nDSM was derived by subtracting the DTM from the DSM, resulting in a raster that represents the true height of all above-ground objects. The results of DTM, DSM and nDSM are shown in Appendix 9.1.

5.2.2 Building footprint extraction

In this study, two sources of building footprints were used: one derived from LiDAR point cloud data and the other obtained from the vector building footprint dataset provided by PICC.

To extract building footprints from the LiDAR data, the first step involved generating a raster layer composed solely of building pixels. This was achieved by filtering the LiDAR points classified under the 'building' category. The sampling value—which determines the pixel size of the resulting raster—plays a crucial role in the quality of the output. A larger sampling value tends to produce more continuous building shapes with fewer internal gaps, but may cause the loss of smaller structural details. Conversely, a smaller sampling value preserves fine geometric features but often results in numerous holes within the building footprint (Appendix 9.2).

After extensive testing, a sampling value of 0.4 meters was selected as the optimal compromise, taking into account LiDAR point density and the building complexity. This choice yielded rasterised building shapes with a satisfactory balance between completeness and geometric accuracy. Nonetheless, the raster layer still exhibited internal voids and jagged, irregular boundaries. Also, certain small elements—such as bicycle sheds or other non-building structures—were included and needed to be filtered out.

To refine the preliminary raster, the following steps were undertaken:

1. Raster-to-vector conversion: The building raster layer was converted into a polygon (vector) format to facilitate further spatial operations.

2. Polygon aggregation: Due to variable point cloud density, some rooftops appeared fragmented, with multiple small polygons representing parts of the same building. These were merged based on a defined aggregation distance, ensuring that adjacent or closely related segments were unified into a single building footprint.

3. Area-based filtering: To eliminate non-building features, an area threshold was established. This involved calculating the area of each polygon, visually inspecting the distribution, and identifying the minimum polygon size that could reasonably represent a real building. Polygons with areas below this threshold were removed. Based on this analysis, a minimum area threshold of 51 square meters was selected.

4. Hole removal: Internal holes within building polygons were eliminated based on a maximum allowable area, determined through visual inspection. Holes smaller than this threshold were filled to improve the solidity of the footprint. After testing, a maximum hole area threshold of 70 square meters was adopted.
5. Boundary regularisation: As a final step, the cleaned building footprints were regularised to smooth the boundaries and improve geometric coherence.

The final cleaned and regularised building footprint layer—along with the vector dataset provided by PICC—is presented in Appendix 9.3.

5.2.3 Segmenting the Building Footprint

Due to the complexity of roof structures in certain buildings—such as variations in height or the coexistence of different roof types—it is necessary to segment existing building footprints to construct more accurate 3D building models.

Although LiDAR point cloud data was initially used to reconstruct building footprints through rasterisation and filtering, the final segmentation and 3D reconstruction were based on the official building footprint dataset provided by PICC. This choice was made after comparing the two sources and evaluating their fitness for LoD2 modelling.

The building footprints derived from LiDAR, although detailed in elevation, exhibited issues such as internal holes, fragmented rooftop polygons, and irregular boundaries that required extensive post-processing. In contrast, the PICC dataset offers topologically clean, pre-generalised, and visually coherent building footprints that are more reliable for segmentation and volume-based modelling. Therefore, to ensure geometric consistency and modelling efficiency, the PICC building footprints were adopted for the remainder of the modelling workflow.

In this study, the segmentation process was based on the vector building footprint data provided by PICC, combined with the DSM generated in Section 5.2.1.

Several key parameters were used to guide the segmentation process:

Spectral Detail: Controls sensitivity to height differences in the DSM. For areas with subtle height variations, higher values improve the detection of those differences.

Spatial Detail: Determines the importance of spatial proximity when forming segments. Lower values result in smoother, more generalised segments, while higher values yield more distinct and independent planes.

Minimum Segmentation Size: Defines the smallest allowable segment size in the DSM.

Regularisation Tolerance: Specifies the maximum linear adjustment allowed when aligning polygon boundaries to right angles or diagonals during geometric regularisation.

Minimum Slope: Sets the minimum slope angle required for a roof surface to be considered sloped.

To obtain optimal segmentation results, multiple parameter combinations were tested iteratively.

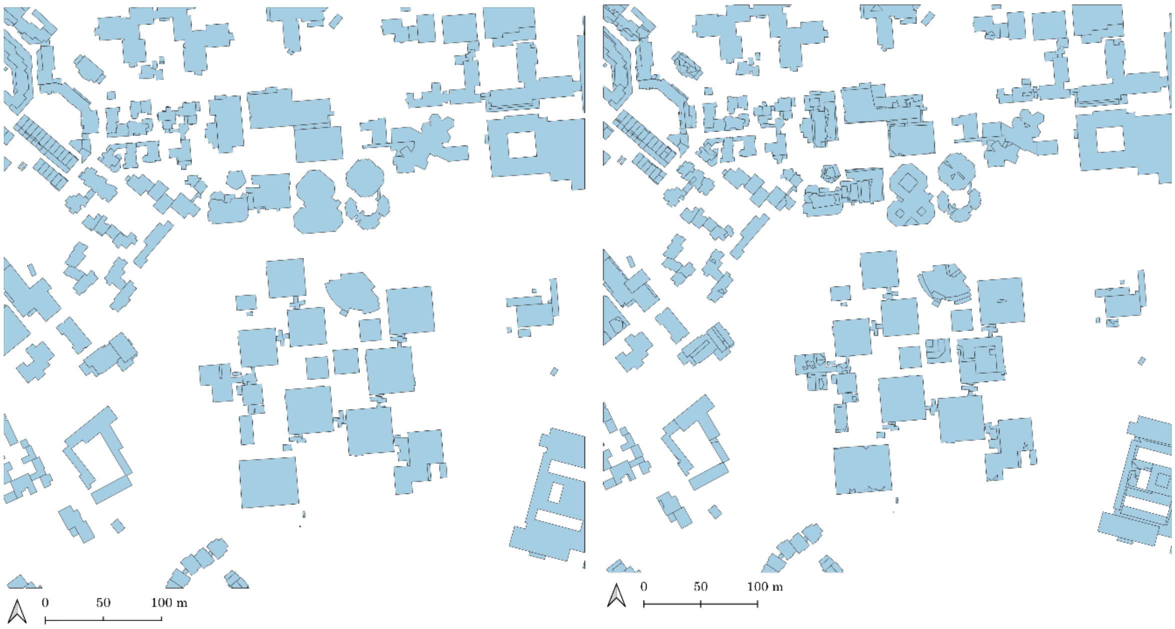

Figure 10 left: Building footprint before segmentation; right: Building footprint after segmentation

Eventually, the following combination was selected based on its overall performance across various roof types:

Spectral Detail = 14, Spatial Detail = 7, Minimum Segmentation Size = 70, Regularisation Tolerance = 0.9, and Minimum Slope = 10 (Fig. 10).

It is important to note that, due to the unique structural characteristics of individual roofs, no single parameter set can perfectly accommodate all buildings. Therefore, the chosen values represent a compromise that performed relatively well for the majority of cases.

5.2.4 Extracting Roof Information

In this step, the objective is to identify flat and sloped planar surfaces within each building's roof area, based on the segmented building footprint layer and the previously derived elevation datasets—the DTM, DSM, and nDSM. By analysing these planar segments, the standard architectural features of the roof are estimated, and the corresponding attribute values are assigned to each roof polygon. These attributes include ridge height, eave height, base height, roof type, and roof orientation.

The extraction process is conducted using automated tools available in ArcGIS Pro. The software analyses the geometry and elevation data of each segmented polygon to infer the most likely roof structure. However, the automatic classification functionality in ArcGIS Pro is limited to a predefined set of roof types: flat roofs, gable roofs, and hip (four-slope) roofs.

While this automated process markedly accelerates the modelling workflow, it may not fully capture more complex or unconventional roof forms. Nonetheless, it provides a reliable basis for assigning essential roof parameters to the majority of buildings in the study area.

5.2.5 Visualising the LoD2 Building Model

At this stage, a segmented building footprint layer with complete roof attributes has been generated. By applying a rule-based symbology file, a LoD2 3D building model can be visualised.

The rule-based symbology is a built-in feature of the 3D Buildings tool in ArcGIS Pro. It uses the roof attribute values extracted in the previous step—such as ridge height, eave height, roof type, and orientation—to render each building in three dimensions. Different rules and calculations are applied automatically according to the specified roof type, allowing for the generation of realistic and structurally accurate roof geometries.

This symbolic rendering enables a consistent and scalable approach to visualise LoD2-level buildings across the entire study area, while preserving architectural distinctions derived from the elevation data and roof segmentation process.

5.2.6 Interactive adjustment supported by Confidence Measurement of the Building Model

After generating the preliminary building model, it was essential to evaluate its reliability by assessing the accuracy of the estimated roof heights. The Root Mean Square Error (RMSE) between the estimated roof heights and the corresponding values in the Digital Surface Model (DSM) is calculated for each building individually.

To avoid potential biases or limitations associated with built-in tools, a custom Python script was developed and executed within ArcGIS Pro's built-in Jupyter Notebook environment. The complete code can be found in Appendix 9.4.

The logic of the RMSE calculation is as follows:

- First, the DSM raster is clipped using the geometry of each building footprint;
- The DSM pixel values within the clipped extent are extracted and converted into a NumPy array;
- The estimated model height is calculated by summing the base elevation (BASEELEV) and the ridge height (BLDGHEIGHT), with adjustments made based on the roof type to better approximate the actual average height of the building.

The height adjustment rules are defined as follows:

- Flat roofs: Height = BASEELEV + BLDGHEIGHT
- Gable and shed roofs: Height = BASEELEV + (EAVEHEIGHT + BLDGHEIGHT) / 2
- Hip and Dome roofs: Empirical scaling factors (e.g., 85%, 70%) are applied to BASEELEV + BLDGHEIGHT to approximate the actual average height, due to a lack of detailed structural data.
- Unrecognised roof types: Default height = BASEELEV + BLDGHEIGHT

The computed RMSE values are then written into the ‘RMSE’ field of the original building footprint layer. These values serve as a critical indicator for assessing model accuracy and guiding subsequent model refinement and validation efforts.

5.2.7 Manual Adjustment of the Building Model

To further enhance the accuracy of the building model—particularly the roof structures, manual adjustments were performed. The shape of the roof in the model is determined by a set of previously computed attribute values, including ridge height, eaves height, roof type, and roof orientation.

While the automatic roof type classification in ArcGIS Pro supports only flat, gable, and hip roofs, the attribute table actually accommodates additional roof types (Fig. 11), such as shed, dome, and mansard roofs. However, due to the limitations of automatic classification, these additional roof types were often misclassified, resulting in discrepancies. For instance, many shed roofs present in the study area were not accurately captured during the automatic process.

To address these inaccuracies, the attribute values were manually adjusted. The correction process was guided by the RMSE values computed in the previous step:

- Buildings with relatively high RMSE values were identified as candidates for manual inspection;
- These models were then visually compared with the original LiDAR point cloud to detect discrepancies in roof shape, orientation, or elevation attributes;
- Attribute values such as ROOFFORM, BLDGHEIGHT, EAVEHEIGHT, and RoofDirAdjust were modified accordingly to better match the observed geometry.

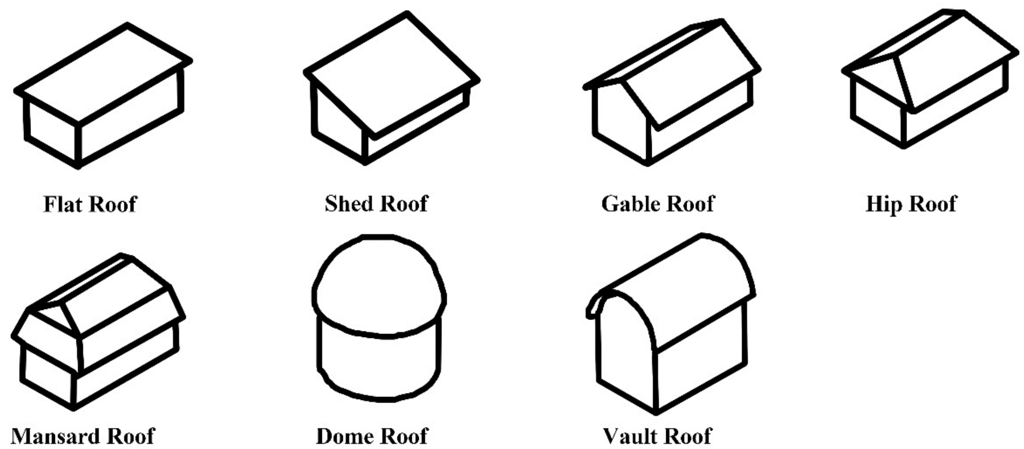

Figure 11 Roof types that can be selected in ArcGIS Pro (source: Esri)

Also, if errors in the segmentation of the building footprint were discovered—such as over-segmentation or under-segmentation—these were corrected by referencing the DSM or orthophoto imagery.

With these refinements, a complete and visually accurate LoD2 building model was achieved.

5.3 Compatibility assessment of building footprints from different sources

As part of the first research objective of this study, it is important to assess the compatibility between building footprints derived from the LiDAR point cloud and those provided by the PICC dataset. This compatibility is evaluated by quantifying the similarity—or, conversely, the difference—between the two sets of building footprints.

To determine the geometric similarity between these two vector datasets, the analysis considers differences in boundaries, dimensions, shapes, and positions. In this study, a composite similarity framework (Ďuračiová, 2023) was adopted that integrates multiple spatial and geometric factors to derive a unified similarity index.

5.3.1 Distance-based similarity

To assess the similarity of object boundaries, shapes, and positions, line distance metrics are employed. These metrics are sensitive to spatial deviations between line geometries.

While traditional point-based distance measures like Euclidean distance are useful, they require the line features to have the same number of vertices, which is not applicable in our case. Therefore, more robust measures were adopted:

- Hausdorff Distance

The Hausdorff distance $d_H(x,y)$ between two line sets x and y is defined as:

$$d_H(x,y) = \max\left(\sup_{x\in X}\inf_{y\in Y} d\,(x,y), \sup_{y\in Y}\inf_{x\in X} d\,(x,y)\right) \quad (2)$$

where sup denotes the supremum (least upper bound) and inf denotes the infimum (greatest lower bound). This metric captures the greatest distance of a point in one set to the closest point in the other. It ensures that two sets are close if each point is near some point in the other set.

- Fréchet Distance

The Fréchet distance $d_F(x,y)$, is defined as the minimum (infimum) over all reparameterizations h of the maximum (supremum) distance between corresponding points on two curves:

$$d_F(x, y) = \inf_{h} \sup_{t} | x(t) - y(h(t))| \quad (3)$$

where x: $[x_1, x_2] \rightarrow R^n$, y: $[y_1, y_2] \rightarrow R^n$ .and sup t |x(t) − y[h(t)]| is the supremum of Euclidean distance |x(t) − y[h(t)]| with respect to t ∈ [x1, x2].

It accounts for both the location and the order of points along the curves, making it well-suited for measuring the similarity between line-shaped geometries.

Because similarity is inversely proportional to distance, distances were converted to similarity scores using:

$$\text{similarity} = \frac{1}{1+\text{distance}} \qquad (4)$$

To standardise the scores to a 0–1 scale (unitless), the transformation was applied:

$$\text{sim\_d} = 1 - \min\left(\frac{\text{d}}{\text{d}_{\text{max}}}, 1\right) \qquad (5)$$

where d is the calculated distance and d_{max} represents a user-defined threshold, such as three times the positional RMSE of the less accurate dataset.

5.3.2 Set-based similarity

In addition to distance-based evaluation, the footprint areas of the two datasets that overlap need to be quantified. This type of comparison is important when evaluating the overall spatial agreement between building shapes, especially in cases where boundary positions differ slightly but the general area is consistent.

Several commonly used set-based similarity indices were selected and calculated from the literature(Ďuračiová, 2023), including:

- Jaccard Index (Intersection over Union):

$$sim\_J(A, B) = \frac{|A \cap B|}{|A \cup B|} \qquad (6)$$

This is one of the most widely used spatial similarity metrics. It provides a straightforward measure of the proportion of shared area relative to the total area covered by either polygon, making it especially useful for evaluating segmentation accuracy.

- Tanimoto Coefficient:

$$sim\_T(A,B) = \frac{|A \cap B|}{|A|+|B|-|A \cap B|} \quad (7)$$

In GIS context, the Tanimoto form is often used as an alternative to the Jaccard Index because it only relies on the area of each feature and their intersection, eliminating the need to compute the union explicitly.

- Sørensen–Dice Coefficient:

$$\mathrm{sim\_SD(A,B)} = \frac{2|\mathrm{A \cap B}|}{|\mathrm{A \cap B}|+|\mathrm{A \cup B}|} = \frac{2|\mathrm{A \cap B}|}{|\mathrm{A}|+|\mathrm{B}|} \quad (8)$$

It is another commonly used statistic to measure the similarity between two sets. It essentially represents the proportion of the intersection relative to the average size of the two sets. This coefficient is often used because it emphasises the shared area between sets and tends to be more robust to differences in the size of individual sets.

Both similarity coefficients range from 0 to 1, and higher values indicate greater similarity between the objects.

5.3.3 Shape-based similarity

Assuming that the area, perimeter, and number of vertices of two areal objects are useful indicators of their similarity—particularly in terms of shape and size, the following similarity indices were defined:

$$\mathrm{sim\_A} = 1 - \frac{|Area_A - Area_B|}{\max(Area_A, Area_B)}$$

$$sim\_P = 1 - \frac{|Perimeter_A - Perimeter_B|}{max(Perimeter_A, Perimeter_B)}$$

$$sim_V = 1 - \frac{|Vertices_A - Vertices_B|}{max(Vertices_A, Vertices_B)} \quad (9)$$

Here, sim_A, sim_P, and sim_V represent the similarity of area, perimeter, and vertex count, respectively. The values for Area_A, Area_B, Perimeter_A, Perimeter_B, Vertices_A, and

Vertices_B refer to the respective geometric properties of polygons A and B. Each index ranges from 0 to 1, with higher values indicating greater similarity.

5.3.4 Aggregated Shape Similarity Index (ASI)

To obtain an overall measure of shape similarity, the above indices were integrated into a single Aggregated Shape Similarity Index (ASI). The ASI combines three core dimensions:

- Distance-based similarity (sim_D), capturing the degree of boundary alignment.
- Set-based similarity (sim_S) measures the extent of spatial overlap.
- Shape-based similarity (sim_SH), reflecting area, perimeter, and vertex differences.

To aggregate these components, fuzzy set theory operators were applied—specifically the MAX (union) and MIN (intersection) functions—since all similarity indices are normalised between 0 and 1. The form of ASI is:

$$\mathrm{ASI} = (\mathrm{simD} \cup \mathrm{simS}) \cap \mathrm{simSH} \qquad (10)$$

In practice, this was further decomposed into specific metrics that correspond to the relevant metrics:

- sim_H: similarity based on Hausdorff distance
- sim_F: similarity based on Fréchet distance
- sim_T: Tanimoto (Jaccard) similarity
- sim_A: area similarity
- sim_P: perimeter similarity
- sim_V: vertex count similarity

Considering that sim_T is typically smaller than or equal to the Sørensen–Dice index (sim_SD), and that sim_H, sim_F, and sim_T together adequately represent both distance-based and set-based similarity, the following simplified formula was adopted:

$$\mathrm{ASI} = \min\,(\max\,(\mathrm{sim\_H}, \mathrm{sim\_F}, \mathrm{sim\_T}), \min\,(\mathrm{sim\_A}, \mathrm{sim\_P}, \mathrm{sim\_V})) \qquad (11)$$

Here, the MAX operator reduces sensitivity to the order of boundary points when assessing distance similarity, while the MIN operator ensures that all geometric descriptors must meet a similarity threshold. This formulation guarantees that a high ASI value is only achievable when both spatial alignment and geometric properties are consistently similar (Ďuračiová, 2023).

5.4 Case Study Analysis

In the case study, a few representative buildings with notably high RMSE values were selected for detailed analysis. The objective is to investigate the potential causes behind their reconstruction errors. To this end, field visits were conducted to directly observe the physical characteristics of these buildings and to compare them against the corresponding 3D models.

By examining these cases, the object is to identify whether the high RMSE is primarily due to structural complexities—such as unusual roof forms, height variations, or architectural details that are difficult to capture using rule-based extrusion methods—or if they result from data limitations, such as insufficient LiDAR point density or inaccuracies in the source polygon layer.

This analysis provides insight into specific conditions under which the modelling workflow may underperform, offering guidance for future improvements or targeted adjustments to the reconstruction process.

5.5 Validation of the Building Model

In this section, the accuracy of the final building model in both horizontal and vertical dimensions was validated.

5.5.1 Horizontal Validation

To assess the planimetric accuracy (in the x and y directions), the high-resolution (4 cm) orthophoto data were used as reference. This dataset is widely considered reliable for spatial validation in urban contexts.

50 sample points were selected randomly within the study area. For each point, the nearest building vertex was identified from three datasets: the orthophoto, the segmented PICC footprint layer, and our manually corrected final building footprint layer. Then the Euclidean distances between the reference dataset (orthophoto), PICC footprints and our model were calculated to obtain the distance errors. The maximum, minimum, average distances, median

and the standard deviation, are computed as performance metrics to evaluate positional accuracy.

This method ensures a balanced assessment by avoiding sampling bias and offers an intuitive metric to quantify spatial deviations. However, potential sources of error include image misregistration, manual digitisation inaccuracies, and differences in delineation methods among datasets.

5.5.2 Vertical Validation

For validating the vertical accuracy, the PICC building roof boundary layer was used, which includes elevation (z) values along each roof edge geometry. Although this z-value is not directly listed in the attribute table, they are embedded in the geometry and can be accessed through geometric calculations in QGIS.

These calculated z-values are then compared with the eave heights of our final building model. For each building, the height error was calculated, including the maximum, minimum, mean, median and standard deviation.

However, this validation method has certain limitations. The z-values derived through geometric computation may carry intrinsic inaccuracies, and the eave height may not fully represent the overall height of buildings with complex roof structures. In addition, the vertical accuracy of the PICC dataset is limited to 25 cm, which may introduce uncertainty in the comparison.

Overall, this two-step validation process allows us to quantitatively assess the spatial alignment and height accuracy of the final building model, ensuring its reliability for further spatial analysis and urban applications.

Chapter 6. Results

This chapter presents the results of the LoD2 building modelling process in Louvain-la-Neuve. It begins with the 3D model generated using PICC building footprints and LiDAR data, followed by an evaluation of model accuracy through RMSE analysis. The relationships between RMSE values and various building characteristics—such as roof type, orientation, height, and area—are examined. The chapter then details the refinement of the model through manual adjustment based on RMSE indicators and compares the performance and geometric differences between PICC and LiDAR-derived footprints. Several high-RMSE buildings are selected for individual case analysis to identify typical modelling errors. Finally, the accuracy of the resulting model is further assessed through both vertical and horizontal validation approaches.

6.1 LoD2 Model

6.1.1 LoD2 Model Obtained by Semi-Automated Modelling

The initial LoD2 building model was generated using the official building footprint dataset provided by PICC as the geometric base, combined with elevation information extracted from LiDAR data. A semi-automated workflow was implemented using the 3D Building tool in ArcGIS Pro, which applies rule-based symbology to reconstruct roof structures based on predefined attributes. Figure 12 presents a visualisation of the resulting 3D model, and Figure 13 shows the model overlaid with the classified LiDAR point cloud for buildings.

Figure 12 LoD2 Model Obtained by Semi-Automated Modelling

Figure 13 LoD2 Model Obtained by Semi-Automated Modelling overlaid with 'Building' LiDAR point cloud

Overall, the model demonstrates a reasonable level of geometric detail, with many buildings accurately segmented into different height levels and roof forms. In particular, buildings with flat and simple structure roofs were generally well-represented, both in terms of shape and alignment with the point cloud. However, the model shows noticeable limitations when dealing with more complex structures—especially those with asymmetric or intersecting roofs, or subtle height variation. These cases often resulted in incomplete segmentation or misclassification of roof forms.

6.1.2 RMSE of roof height

To quantitatively assess the geometric accuracy of the semi-automated building model and support further improvements, the RMSE values are calculated from the generated LoD2 model and the LiDAR-derived DSM. These values reflect the vertical discrepancy between them and help identify the buildings with the highest errors for further inspection and refinement. A summary of the RMSE distribution is presented in Figure 14.

The RMSE values predominantly fall between 0 and 2 meters, suggesting generally acceptable accuracy. However, a few outliers range from 4 to 6 meters, which are typically due to incorrect roof type assignment or the presence of frequent, small height variations that were not accurately captured by the tool. The minimum RMSE recorded was 0.09 m, indicating excellent alignment with the LiDAR data for certain buildings. The maximum value reached 6.31 m, suggesting substantial discrepancies likely caused by incorrect roof type identification, inaccurate height estimation, or poor segmentation in areas with structural complexity.

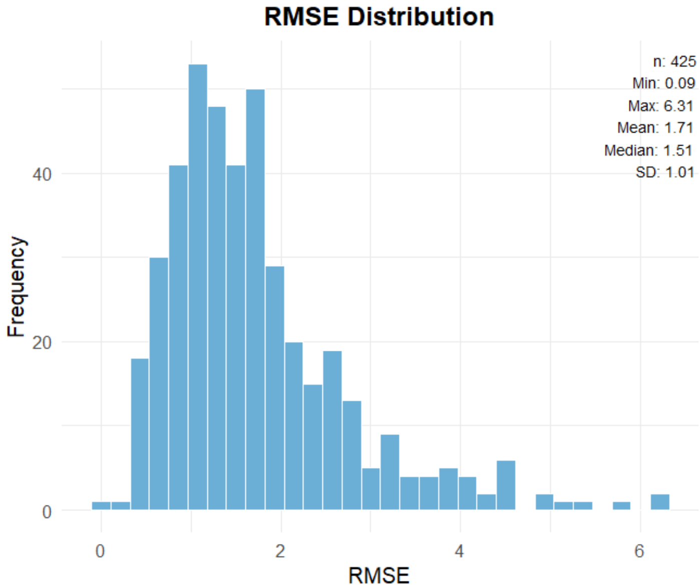

Figure 14 Distribution of RMSE values (in meters) between the generated LoD2 model and LiDAR-derived DSM, including statistical indicators

The average RMSE was 1.71 m, and the median was 1.51 m. The mean being slightly greater than the median suggests a right-skewed distribution, influenced by a small number of buildings with large errors. The standard deviation of 1.01 m reflects moderate variability across the dataset.

While these general statistics provide a global overview, a more detailed analysis was conducted to investigate how specific building attributes might influence RMSE values. The factors examined include roof type, building height, roof orientation, and building footprint area.

- Roof Type:

Table 4 shows the statistical values of RMSE by roof form, and Figure 15 displays a boxplot comparing RMSE distributions for different roof types: flat, gable and hip. As expected, flat roofs are the most common, followed by gable roofs, while hipped roofs are the least represented. Flat roofs exhibited the lowest minimum, mean, and median RMSE values, indicating better overall performance in height alignment. However, they also showed the widest range and the most outliers, with the highest maximum RMSE observed among all roof types. This duality reflects two tendencies: flat roofs with minimal height variation are easier to model accurately, while others may be misclassified for the roof type or oversimplified for the height variation, leading to large deviations. Gable roofs had moderate mean and median values with a relatively smaller standard deviation. Hip roofs had the highest median RMSE, likely due to the fact that typical hipped roofs are rare in the study area, and the software may have incorrectly labelled complex or intersecting roof structures as hipped roofs, increasing the likelihood of modelling error. These patterns reflect differences in modelling performance across roof types.

Table 4 Statistical values of RMSE by roof form

Roof form	Count	Min	Max	Mean	Median	SD
Flat	371	0.09	6.31	1.69	1.43	1.05
Gable	53	0.61	3.78	1.81	1.65	0.65
Hip	6	1.70	3.42	2.42	2.20	0.76

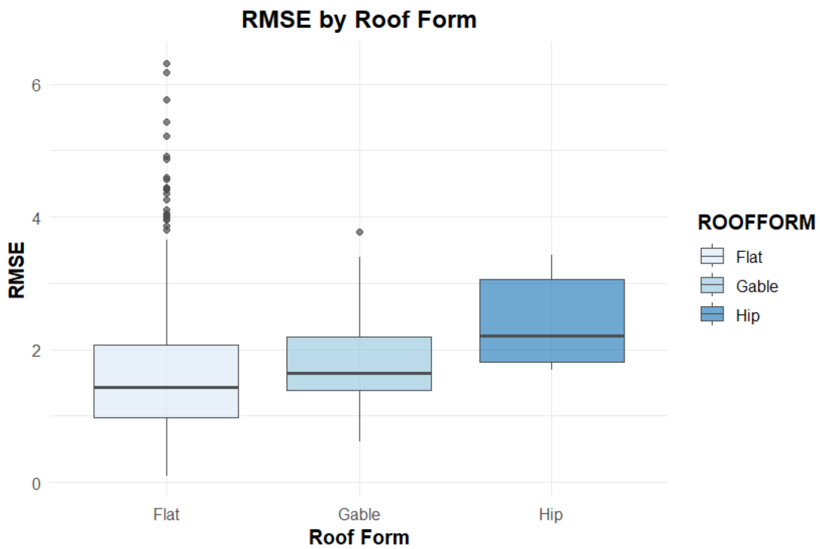

Figure 15 Boxplot comparing RMSE distributions for different roof types

➢ Building Height:

As shown in Figure 16, no strong linear relationship was observed between building height and RMSE. Most buildings with RMSE values greater than 5 meters had heights in the 15–25 meter range, though high RMSEs were not exclusively associated with taller buildings. Flat roofs spanned all height ranges, while gable and hipped roofs tended to fall within the 5–20 meter range.

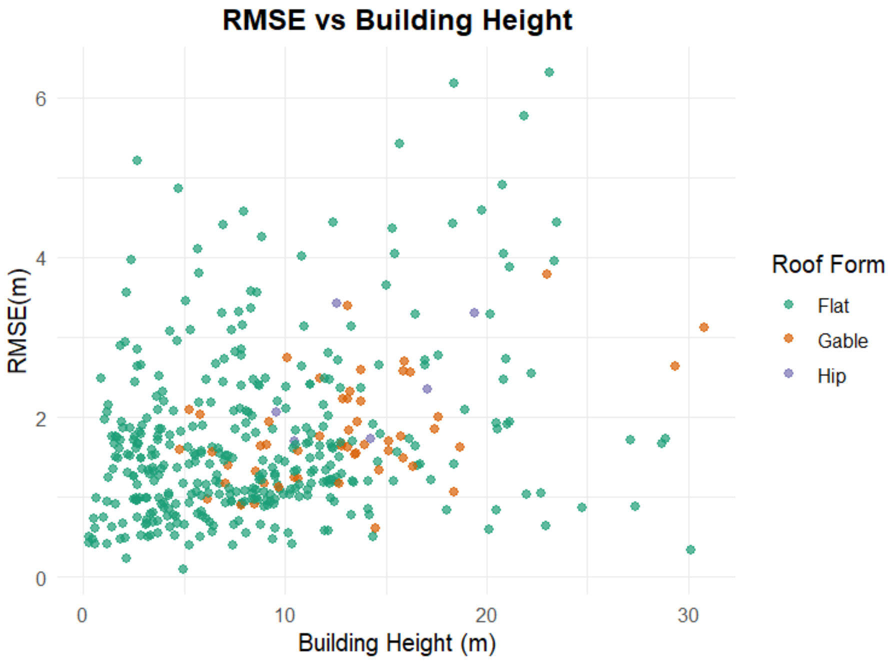

Figure 16 Scatter plot comparing RMSE distributions for different building height

➢ Roof Orientation:

Figure 17 shows the comparison of RMSE values across different roof orientations, excluding flat roofs (which have no orientation). The average RMSE across most orientation angles was below 2 meters, with the exception of buildings with roof directions around 90°, which showed slightly higher average errors. However, the variation across orientations was relatively small, and no strong correlation was observed.

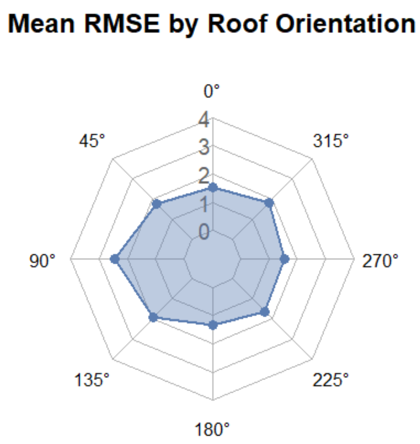

Figure 17 Wind Rose Chart comparing RMSE distributions for different roof orientation

➢ Building footprint Area:

The relationship between building footprint area and RMSE is presented in Figure 18. Most buildings had areas between 0–250 m². For buildings larger than 250 m², RMSE values were mostly below 2 meters, with only a few exceeding 4 meters. Buildings with smaller floor areas showed a broader range of RMSE values, with several exceeding 4 or even 6 meters. These structures often correspond to auxiliary components like corridors, stairwells, or elevator shafts—small but vertically complex elements that are difficult to model precisely. Their limited surface area and height discontinuities make both segmentation and elevation assignment more error-prone.

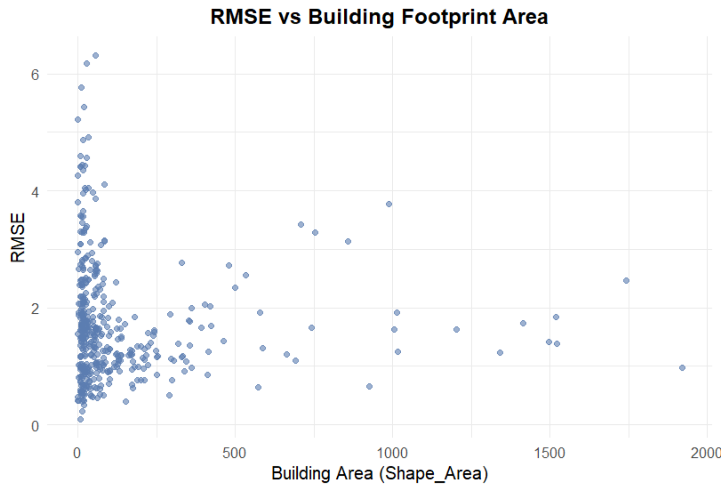

Figure 18 *Scatter plot comparing RMSE distributions for building footprint area*

6.1.3 Adjusted LoD2 Model

Following the RMSE analysis, a subset of buildings with the highest error values was manually reviewed and modified to enhance the model's geometric accuracy(Fig.19). Figure 20 shows

Figure 19 spatial distribution of RMSE the updated LoD2 model after manual adjustments, Figure 21 shows the model visualised alongside the classified LiDAR point cloud.

While the majority of buildings remained unchanged due to acceptable RMSE values, manual corrections were applied to a limited number of buildings with complex roof structures or visible inconsistencies. Adjustments included re-segmentation of roof sections and refinement of eave as well as bldg heights through visual comparison with the LiDAR data.

The RMSE values of the edited buildings decreased following these modifications, with improved geometric alignment observed. A detailed analysis of specific buildings is presented in Section 6.3(Case Study).

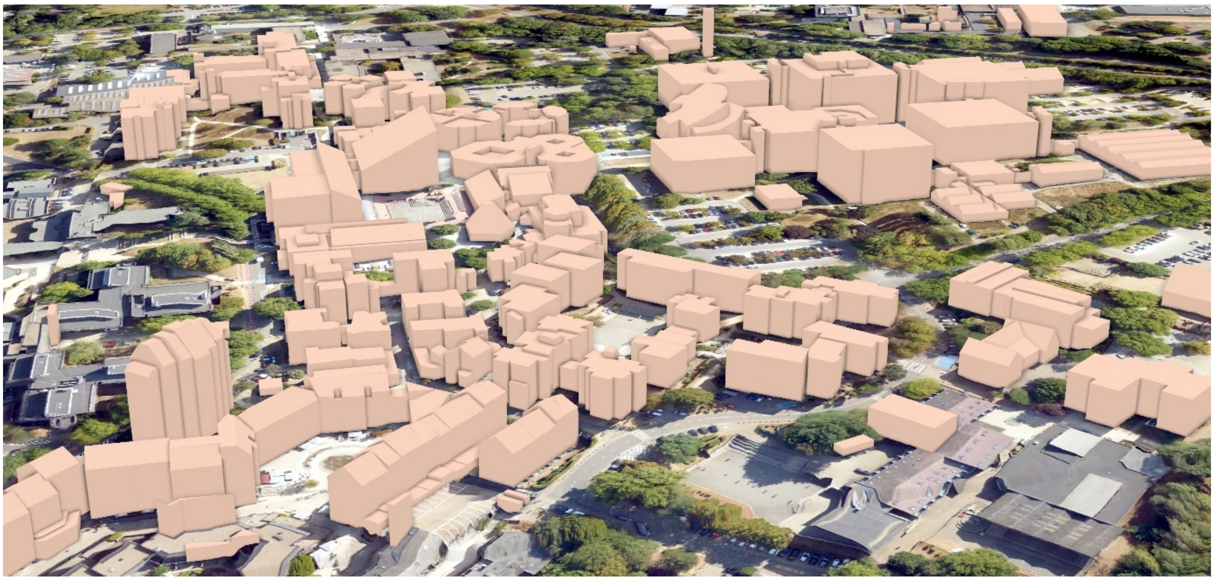

Figure 20 Adjusted LoD2 Model

Figure 21 Adjusted LoD2 Model overlaid with 'Building' LiDAR point cloud

6.2 Compatibility Assessment of Building Footprints

The similarity comparison between the building footprints extracted from the LiDAR point cloud and those from the PICC was conducted using the aggregated similarity index which includes three sub-indices: distance similarity (sim_d), set similarity (sim_s), and shape similarity (sim_sh). Figure 22 illustrates the footprints from both datasets within the study area, along with their corresponding aggregated similarity scores, which show good general agreement. Most primary buildings are correctly captured in both sources, and their overall shapes are consistent. However, some smaller auxiliary structures appear in the official dataset but are missing from the LiDAR-derived version. Further inspection revealed that these structures were not classified under the "building" category in the LiDAR point cloud and were

Figure 22 LiDAR derived footprints and PICC footprints with their similarity indices

instead labelled as “unclassified.” This likely results from classification thresholds that exclude structures with low elevation, small footprint areas, sparse point coverage, or incomplete shape due to occlusions such as vegetation. In addition to omissions, the LiDAR-derived footprints tend to exhibit jagged or irregular boundary edges, especially for buildings with non-orthogonal outlines. This is a known limitation in building extraction from point clouds. Although a regularisation step was applied to smooth the geometry, some boundary irregularities remain.

Summary statistics for each similarity metric are presented in Table 5.

Table 5 statistical values of Aggregated Similarity Index

	Min	**Max**	**Mean**	**Median**	**SD**
Sim_d	0.27	0.97	0.78	0.84	0.16
Sim_s	0.00	0.96	0.64	0.80	0.33
Sim_sh	0.00	1.00	0.68	0.82	0.31

All three similarity measures exhibited a wide range of values. The minimum values were notably low: both the set similarity and shape similarity reached 0 in some cases, indicating that certain buildings were poorly matched between the two datasets. In contrast, the maximum values for all three metrics exceeded 0.95, and the maximum shape similarity reached 1.0, reflecting a high degree of fit for some buildings.

The mean values of the three sub-indices were all approximately 0.7, with distance similarity having the highest mean and set similarity the lowest. The median values were slightly higher, around 0.8 for all three indices, suggesting that the overall distribution is right-skewed, with a subset of poorly matched cases pulling the mean downward.

In terms of variability, distance similarity had the lowest standard deviation (0.16), indicating a more concentrated distribution of values. Both set similarity and shape similarity had standard deviations around 0.3, suggesting a more dispersed distribution. These patterns are clearly depicted in the boxplots in Figure 23. Most distance similarity values exceeded 0.5, with relatively few outliers below that threshold. In contrast, set and shape similarity displayed a broader range and a higher number of values below 0.5, indicating greater variability in performance.

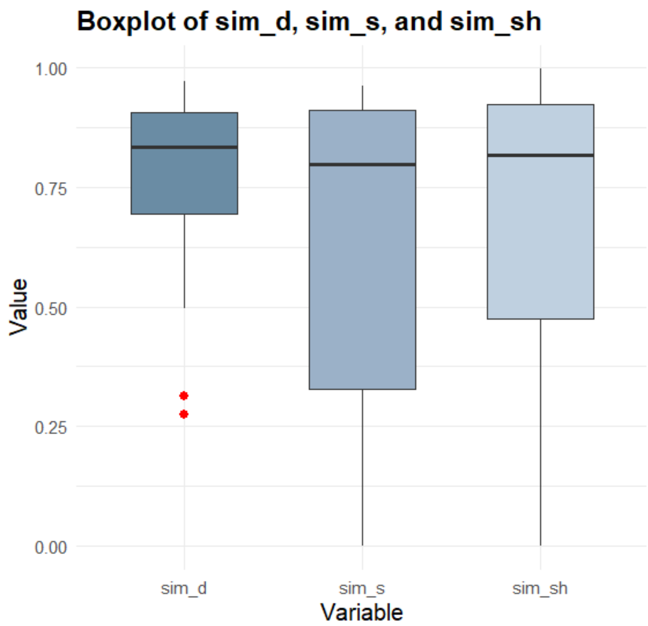

Figure 23 Boxplot of sim_d, sim_s and sim_sh

The distribution of the aggregated similarity index is visualised in the histogram in Figure 24, and its classification into five equal intervals, as well as the summary statistics, are shown in Figure 25. The aggregated similarity values mostly ranged between 0.6 and 1.0, but a non-negligible proportion of outliers had values close to 0. These extremely low values suggest significant mismatches in certain building footprints. many of these outliers occur in densely built areas composed of several interconnected structures, such as main buildings linked by corridors or elevator shafts. The complexity of these linkages often leads to missegmentation in the LiDAR-derived footprints, resulting in reduced set similarity and, consequently, lower aggregated similarity.

Another group of low-similarity cases involves buildings with curved or angled boundaries. In such cases, the jaggedness of LiDAR-based outlines can strongly affect distance similarity. When combined with misclassification or poor segmentation in clustered areas, the result is a further drop in the aggregated similarity score

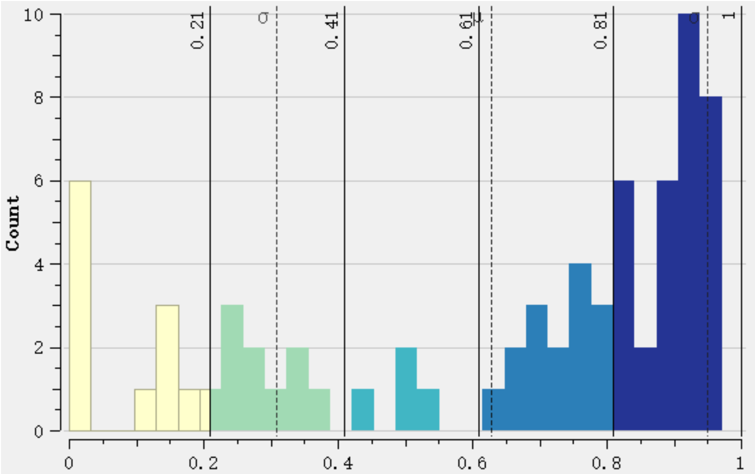

Figure 24 Histogram of aggregated similarity index

Figure 25 classification of aggregated similarity index and its summary statistics

6.3 Case Analysis

To better understand the sources of error in the automatically generated LoD2 models, a set of representative buildings with the highest RMSE values—calculated in section 6.1.2—were selected for detailed analysis. Figure 26 illustrates the locations of the four selected buildings across the study area. The analysis focuses on identifying specific locations where deviations occurred and exploring the related geometric features. Table 6 summarizes the key characteristics of these buildings, including their RMSE values before and after manual refinement.

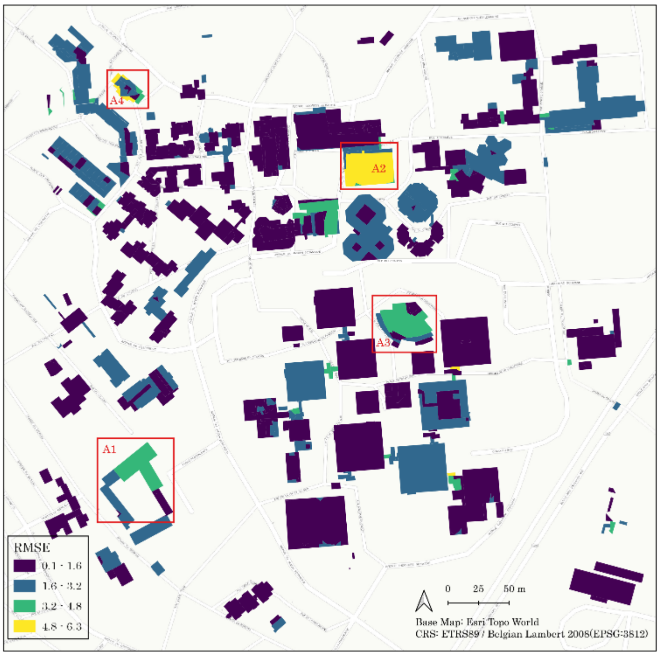

Figure 26 Locations of high RMSE buildings discussed in table 6

Table 6 characteristics of the selected buildings

		Highest RMSE before	Everage RMSE before	Highest RMSE after	Everage RMSE after
A1	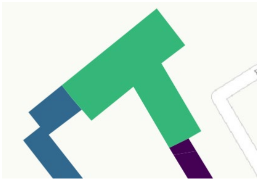	3.42	1.82	2.17	1.56
A2	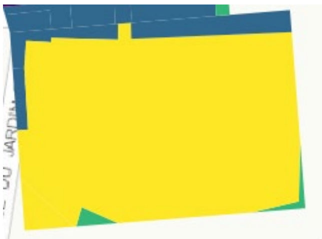	6.17	3.79	6.24	3.33
A3		3.29	1.7	2.68	1.64
A4	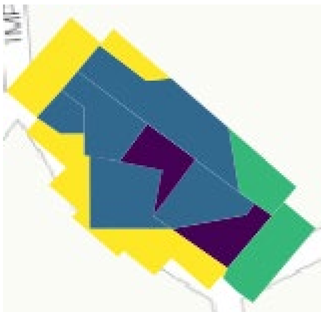	6.31	3.06	7.04	3.98

Each selected building represents a single architectural entity that was internally subdivided during the modelling process. Although the RMSE values of some subdivided sections were relatively moderate, certain segments exhibited exceptionally large errors. To comprehensively assess such cases, the entire building containing the high-error section was analysed.

Building A1 (Ferme du Biéreau concert hall) had a maximum initial RMSE of 3.42 meters. This error occurred at the junction of two intersecting roof sections at a corner of the building (Figure 27).

Figure 27 Building A1 in orthophoto

A visual comparison between the model and the LiDAR point cloud revealed a misclassification of the roof geometry. In the original building footprint, this section was represented as a single, undivided entity and was automatically assigned a hip roof type. This classification likely resulted from the tool's limitations when processing interlocked structures: when two buildings intersect and the footprint remains undivided, and the roof geometry includes slopes in multiple directions, the tool defaults to classifying it as a hip roof. While in reality, both volumes are gable-roofed buildings with a more pronounced height difference than reflected in the automated model. The modelling tool failed to capture this nuance, treating the entire structure as a single roof plane with gradual slopes in all directions. This misinterpretation directly impacted the RMSE because of how roof height is computed in the modelling tool: for hip roofs, the height is taken as 85% of the average of ridge and eave heights, whereas for gable roofs, the height is calculated as 50%. Therefore, even if the actual ridge and eave heights were relatively accurate, the incorrect roof type assignment alone could lead to significant height discrepancies.

Furthermore, because the building footprint was not segmented, the model applied the ridge and eave values of the taller of the two volumes to the entire structure. While this may not have introduced substantial error for the taller section, it led to an overestimation of height for the lower building. This compounded the RMSE for the entire building footprint, especially at the junction where the difference in height and roof orientation is most pronounced.

After manual segmentation and correction, the RMSE for this part decreased to 2.17 meters, and the roof geometry better aligned with the LiDAR point cloud (Figure 28).

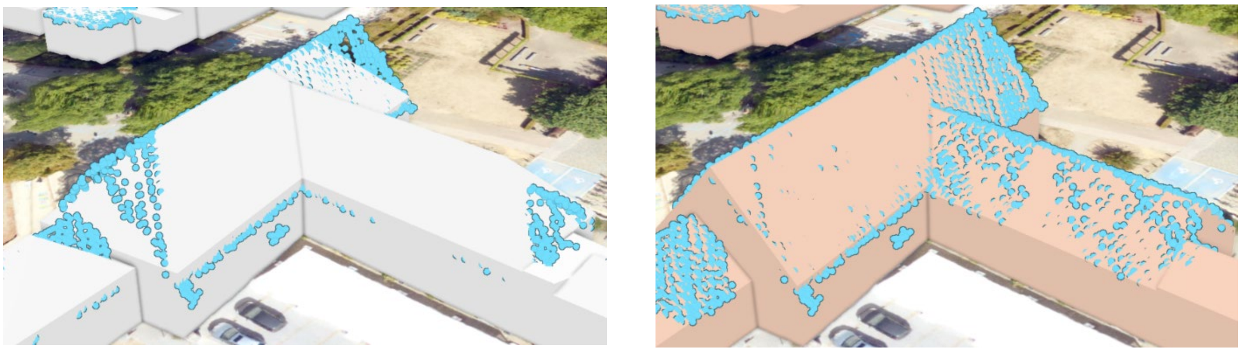

Figure 28 left: initial model with LiDAR point cloud; right: model after manual editing with LiDAR point cloud

Building A2 (Musée building, emblematic LLN building) Building A2, Musée L, is a museum where significant RMSE values were observed across the entire structure, with especially pronounced errors occurring along its peripheral sections (Fig. 29). A closer look at the original building footprint reveals that three irregular, sharply angled, and very small polygons were segmented along the edges. These likely correspond to minor structural protrusions resulting from the building's unique architectural design.

Figure 29 (a)Building A2 in orthophoto;(b) error-prone side of Building A2

Beneath the main roof, several small rectangular platforms of varying height are present. While most of these are located underneath the eaves of the main structure, some portions extend outward beyond the roofline. On another façade, several subsidiary elements protrude with enough width to be identifiable as separate roof surfaces from a top-down perspective, even though their heights are noticeably lower than that of the main structure. This configuration poses a substantial challenge to the segmentation process. The small surface area and subtle height changes require a denser point cloud to be accurately detected and properly segmented. However, the point density in this area was insufficient to resolve such fine-grained details.

In the automatically generated model, roof type classification was inconsistent. The main section was misclassified as a gable roof, while the edge fragments were labelled as flat roofs. In reality, the main roof is a shed roof, which was not among the types successfully recognised by the tool. As a result, it defaulted to assigning the more probable gable roof category instead.

Furthermore, the small roof-like platforms located below the main roof's eaves—which extend outward but do not strictly constitute independent roof structures—were too minor in scale to be treated as distinct segments in the modelling process. In the subsequent manual correction, the building was treated as a single, unified shed roof structure for simplification, as this approach offered a more accurate representation of the LiDAR point cloud geometry and reduced the RMSE substantially. After manual adjustments, the RMSE dropped to 3.77 meters, and the roof geometry more closely matched the LiDAR point cloud (Figure 30).

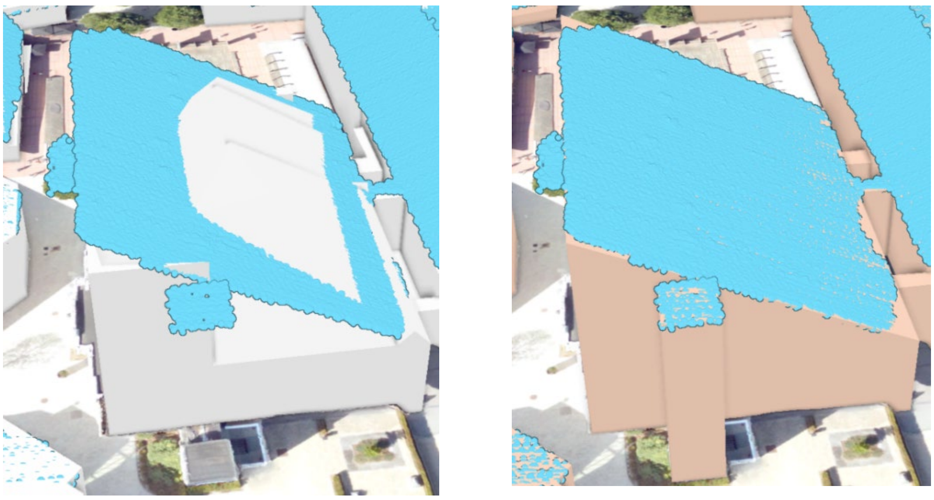

Figure 30 left: initial model with LiDAR point cloud; right: model after manual editing with LiDAR point cloud

Building A3 (South Auditorium building) Building A3 is an educational facility where the highest RMSE values were concentrated in the main body of the structure, with additional large errors observed along its peripheral segments. The building has a relatively complex form. From the perspective of footprint segmentation, the original process was generally successful in separating the main structure from smaller auxiliary components. However, some issues persisted in segmenting the smaller peripheral areas.

Figure 31 Building A3 in orthophoto

In certain zones, abrupt changes in elevation led to incorrect divisions, where a continuous surface was mistakenly split into two parts. In other sections, height variation was less pronounced, and dense vegetation around the building introduced further inaccuracies by obstructing the LiDAR signal, resulting in imprecise boundary delineation.

Regarding roof classification, A3 shares similarities with A2 in that it features a shed roof misclassified as another type. However, unlike A2, Building A3 does not exhibit a typical shed structure. A standard shed roof is a single planar surface, bounded by straight ridge and eave lines. In contrast, the ridge and eaves of A3 are both curved, creating a concave, downward-sloping roof surface rather than a flat plane. This curved shed form is not supported among the available roof types in the modelling tool used in this study. A similar situation applies to the smaller attached roof segments along the edges, which also display a curved shed profile.

The observed RMSE errors are likely attributable to the mismatch between the actual roof geometry and the assumed geometry used in classification and height calculation. Since the tool computes building height differently based on roof type, applying an incorrect roof type to a non-planar surface inevitably introduces significant discrepancies between the model and the LiDAR point cloud.

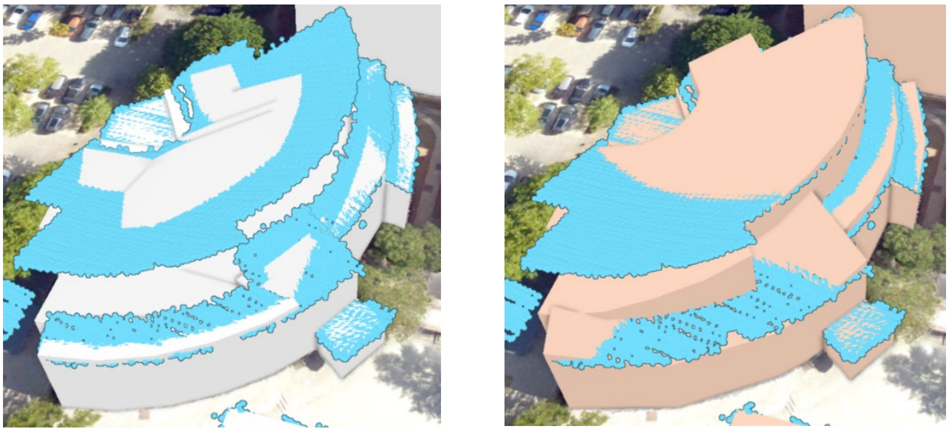

Figure 32 left: initial model with LiDAR point cloud;right: model after manual editing with LiDAR point cloud

Building A4 had the highest RMSE in the entire study area, reaching 6.31 meters. The maximum error occurred at the building's edge, and other areas with large RMSE values were also located around the periphery (Figure 33). The building consists of several adjoining units with similar structural forms but varying heights, which presents a considerable challenge for accurate roof segmentation.

Figure 33 left: Building A4 in orthophoto; right: RMSE class of A4 building (yellow represents the highest value, followed by green, blue, purple)

The original segmentation performed poorly, largely due to the presence of numerous small substructures within the complex and only subtle differences in elevation between them. Accurate modeling would require first delineating each individual unit, followed by detailed segmentation of their respective roof structures. However, such segmentation is beyond the capabilities of the tool used in this study. Neither elevation differences nor spectral information were sufficient to clearly separate the individual units, as all components share nearly identical structural forms and materials.

Due to the inaccuracies in segmentation, the resulting roof type classifications for this building are largely unreliable. Aside from a central section correctly identified as a flat roof, most areas were misclassified as either flat roofs or gable roofs, whereas the actual form should be closer to a shed roof. Even in the correctly labeled flat roof section, the segmentation was imprecise due to the subtle and gradual height changes between units, leading to height mismatches when compared to the LiDAR data.

In reality, the building presents as a series of interconnected structures, each resembling a gable roof, arranged in a row with heights gradually decreasing from the center towards the sides. However, unlike a typical gable roof, the ridge line across the top of the complex forms a flat horizontal surface. This hybrid configuration—sloped yet flattened at the ridge—is not supported by the roof typologies available in the modeling tool, which contributes further to the observed geometric mismatch and high RMSE values.

After manual corrections, the roof geometry became better aligned with the LiDAR point cloud(Figure 34).

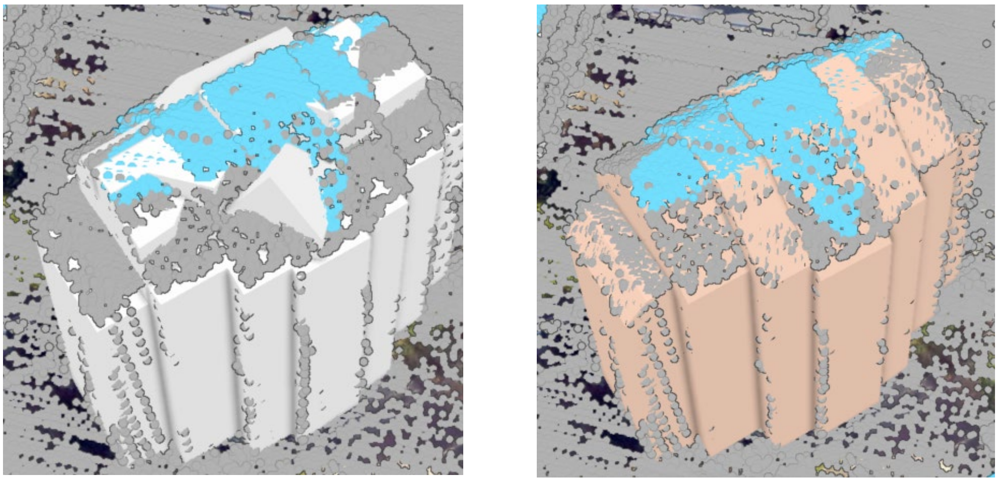

Figure 34 left: initial model with LiDAR point cloud; right: model after manual editing with LiDAR point cloud (blue: classification 'building'; grey: classification' unassigned')

- Additional Observations

In addition to these complete buildings, there are several smaller building parts in the study area with very high RMSE values. These are often connectors between two buildings, such as corridors, elevator shafts, or entrance halls (Fig. 35). These components were mostly classified as flat roofs, which aligns with reality. However, the main sources of error lie in segmentation and elevation assignment. These segments are usually very small in area and exhibit slight elevation differences compared to the adjacent main structures. This makes accurate segmentation more difficult, which in turn leads to misidentification of point cloud heights in the corresponding areas, resulting in vertical discrepancies.

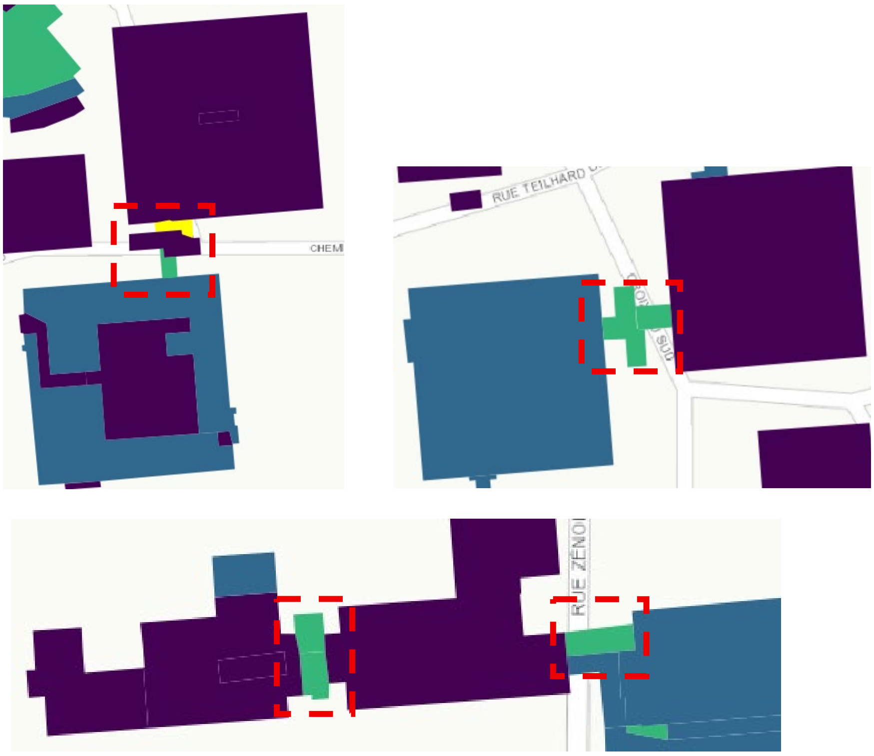

Figure 35 Example of high RMSE in small building parts

6.4 Validation of the Building Model

6.4.1 Horizontal Validation

To assess the horizontal accuracy of the model, 50 random points were selected and paired with their closest corresponding vertices from three datasets: orthophotos, segmented PICC building footprints, and manually refined modelled building footprints. The distances between each pair were computed, and the results of the pairwise comparisons are presented in Table 7.

Table 7 Statistical Summary of Pairwise Horizontal Distances Between Orthophoto, PICC, and Building

Model Footprints (in meters)

	Min	Max	Mean	Median	Standard Deviation
Orthophoto-PICC	0.035	2.604	0.34	0.241	0.395
Orthophoto-final	0.041	2.706	0.313	0.215	0.399
PICC-final	0.000	2.561	0.169	0.0006	0.525

The minimum distances between the orthophoto and PICC points (0.035 m) and between the orthophoto and the final model points (0.041 m) both suggest a good geometric fit. The maximum values, 2.604 m and 2.704 m respectively, indicate the presence of a few mismatched vertices or potential segmentation errors in the building outlines. The mean distances in both comparisons are approximately 0.3 m, with medians around 0.2 m. In each case, the mean exceeds the median, suggesting the influence of a small number of outliers. Standard deviations are around 0.4 m, reflecting a moderate degree of dispersion in the measurements.

Since the final model's footprints were derived directly from the PICC dataset with manual adjustments, their mutual comparison yields the best results among the three combinations. This pair shows a minimum value of 0 m, indicating perfect alignment in some locations, and a maximum of 2.561 m, confirming that some discrepancies still exist. The mean distance is 0.169 m and the median is only 0.0006 m, both markedly lower than those in the other comparisons. Again, the mean is greater than the median, pointing to the presence of a few larger errors. The standard deviation of 0.525 m also suggests a moderate level of variation.

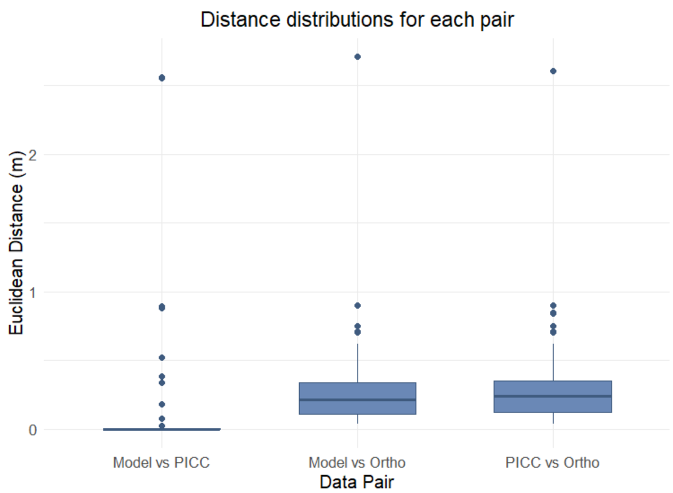

Figure 36 Boxplot of the distance distributions for each pair

Figure 36 presents a boxplot of the distance distributions. The errors between the model and

PICC points are highly concentrated near zero. Errors in the comparisons between the model and the orthophoto, as well as between the orthophoto and PICC points, are similarly concentrated and mostly fall below 0.4 m. These results indicate that the model aligns most closely with the PICC footprints and also maintains a good level of agreement with the orthophoto.

To summarise, the three datasets have a generally high degree of consistency. The modelled building footprints and the PICC data exhibit the closest alignment, with both also demonstrating good agreement with the orthophoto. This confirms the reliability of using the official PICC dataset as the basis for further processing. Discrepancies observed in a few individual cases may stem from differences in how building footprints are segmented across datasets, which can lead to the identification of different nearest vertices and thus to variations in calculated distances

6.4.2 Vertical Validation

Vertical accuracy was evaluated by comparing the eave heights from the PICC dataset with those derived from the adjusted building model. The differences were calculated by subtracting the PICC values from the modelled heights. Since the differences can be both positive and negative, first, the absolute values were taken to represent the magnitude of error without implying direction. Smaller values indicate better vertical alignment.

Table 8 Statistical features of absolute vertical errors

Min	Max	Mean	Median	Standard Deviation
0.000	23.643	2.867	0.938	4.402

Table 8 summarizes the statistical properties of these vertical errors. The minimum value is 0, demonstrating that some buildings are perfectly aligned in terms of eave height. The maximum value reaches 23.643 m, highlighting significant discrepancies for certain buildings. The mean error is 2.867 m, while the median is 0.938 m. As the mean is considerably larger than the median, this again suggests that a small number of large errors skew the average. The standard deviation of 4.402 m reflects a notable degree of dispersion in the dataset.

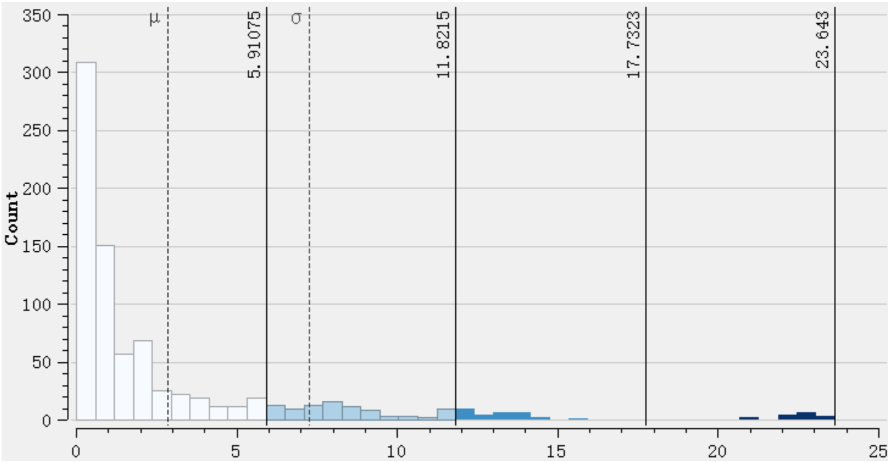

Figure 37 Histogram of absolute vertical errors

Figure 37 shows the histogram of vertical errors. Most values fall within the range of 0 to 5 m, with a peak near 0, indicating that the majority of buildings are vertically consistent with the PICC data. However, a few outliers exceed 20 m. One of the primary causes appears to be segmentation inconsistencies in the roof area. For instance, in the case of Building A3, the model divides the structure into several smaller components, while the official data treats the building as a single entity. Also, the building features a non-standard roof form—similar to a gable roof but with a flat ridge—which leads to misinterpretation of eave heights in the model, further contributing to the error. The high average error associated with shed roofs is primarily due to this particular structure, where multiple sloped sections exhibit large discrepancies.

Figure 38 presents the average vertical error by roof type. Among the different categories, sloped roofs exhibit the highest average error. The error associated with four-slope roofs is slightly lower. Flat roofs and gabled (mountain wall) roofs have similar mean errors, both below 3 m.

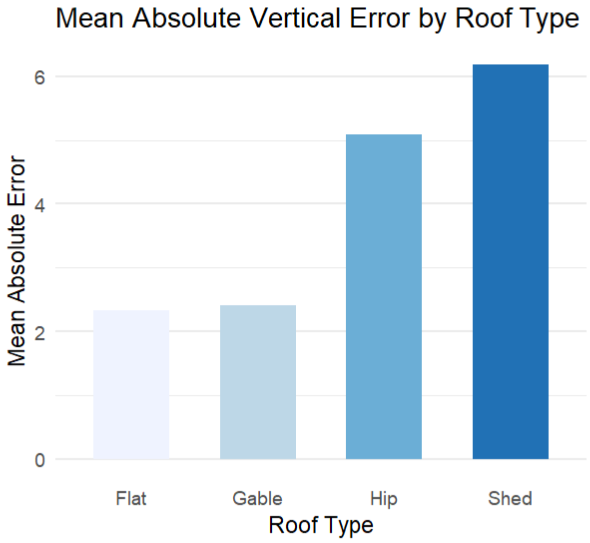

Figure 38 Absolute average vertical error by roof type

The distribution of actual vertical errors is illustrated in Figure 39. Most values are clustered around zero, indicating overall accuracy. Among the larger deviations, the majority of negative errors fall within the range of –10 to 0, with only a small number exceeding –10. On the positive side, most values lie between 0 and 10, although a few outliers exhibit greater deviations, with the maximum exceeding 20.

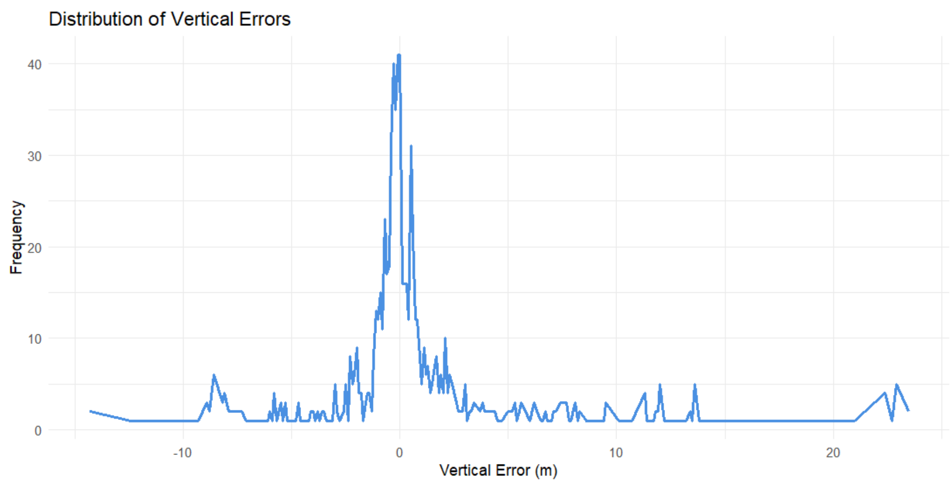

Figure 39 Distribution of actual vertical errors

Chapter 7. Discussion

This chapter summarises the key findings of the study concerning the initial research questions. It reflects on the strengths and limitations of the modelling approach and highlights major sources of uncertainty. The discussion also explores potential improvements, as well as implications for future applications.

7.1 LoD2 Model

This study employed the 3D Buildings tool in ArcGIS Pro to construct the LoD2 building model, using LiDAR point cloud data as the sole input. The modelling workflow is semi-automated: the tool integrates footprint generation, segmentation, and roof assignment into a streamlined process that requires minimal manual operation. From a usability perspective, this greatly reduces the workload and technical threshold for producing 3D models. However, the internal modelling logic of the tool is encapsulated, and users can only rely on software documentation to infer how decisions—such as roof type assignment or segmentation thresholds—are made. This black-box nature can introduce uncertainty in the modelling outcome, especially in complex urban environments.

One key limitation observed during the modelling process is the restricted classification of roof types (Tarsha-Kurdi et al., n.d.). Although the tool supports multiple roof categories, the automatic step consistently assigned only three types: flat, gable, and hipped roofs. As the study area includes a wider variety of complex or irregular roof forms—such as stepped, curved, or intersecting roofs—this simplification frequently led to misclassification. Manual correction was therefore necessary to improve the structural fidelity of the resulting models.

To better understand what factors contributed to high RMSEs, several potential influences were analysed, including roof type, building height, roof orientation, and building footprint area. Based on the results, roof type classification and building footprint area are the two factors that most strongly influence RMSE. Errors related to roof type stem from the limited classification capabilities of the automated tool, while issues with footprint area are often linked to small, complex substructures that are inadequately captured during segmentation. Manual corrections in the modelling process were therefore targeted at these specific issues to improve overall accuracy.

7.2 Comparison of Building Footprints

This study utilised two sources of building footprint data: one extracted from the LiDAR point cloud and the other derived from official PICC datasets. Each source has distinct characteristics. The PICC dataset provides detailed and cartographically validated urban features, offering high positional accuracy and consistency across the study area. However, it lacks elevation attributes and contains no information on roof geometry. In contrast, LiDAR data provides three-dimensional information, enabling the estimation of actual roof heights and shapes, which are essential for LoD2 modelling. Nevertheless, this 3D capability comes with challenges, such as classification errors and inconsistencies in footprint extraction.

To determine whether the LiDAR-derived footprints were accurate and complete enough to serve as a modelling base, a similarity analysis was conducted. This comparison evaluated the spatial agreement between the two datasets in terms of footprint geometry and coverage.

The results show that overall similarity is high, with the majority of LiDAR-derived footprints closely matching their PICC counterparts. However, certain discrepancies were observed. In particular, the LiDAR-based approach failed to detect several small and isolated structures due to classification omissions. Also, segmentation issues emerged in buildings with more complex structures, such as those featuring internal courtyards, elevator shafts, or connecting corridors. In such cases, parts of a single building were sometimes misclassified as separate units or omitted altogether.

These limitations in the LiDAR-derived dataset motivated a methodological shift. While the LiDAR footprints offered greater detail in vertical geometry, they lacked the completeness and reliability required for consistent large-scale modelling. Therefore, the more accurate and geometrically stable PICC dataset was selected as the final source for building footprints, while LiDAR continued to play a key role in assigning roof heights and forms.

This evolution in data usage—starting with an initial reliance on LiDAR for both footprint and elevation data, and later integrating PICC for horizontal footprint accuracy—reflects a critical decision in balancing data precision and modelling feasibility. It also highlights the importance of dataset complementarity in 3D city model construction.

7.3 Case Study

Based on the case analysis above, several potential factors contributing to large RMSE values can be identified. First, errors are more likely when the structure is not a single building but a combination of multiple interconnected buildings with subtle height differences. Such configurations complicate roof segmentation, especially when the segmentation is based on height gradients and spectral characteristics. In cases where materials are similar and height differences are minimal, segmentation may become inaccurate, leading to incorrect roof type classification and subsequently to modelling errors.

Another important factor is the limitation of the tool itself. In the automatic classification of roof types, the tool is restricted to only three options: flat, gable, and hip roofs. This constraint causes many shed or irregular roof types to be misclassified into one of these three categories, introducing further errors. Also, small architectural features beneath the eaves or on exterior walls frequently lead to large errors. These elements often have a small footprint but differ slightly in height from the main roof, making them difficult to detect and classify correctly.

Lastly, more complex roof forms that do not exist in the tool's predefined typology—such as curved, compound, or hybrid roofs—also contribute to higher RMSE values, as the modelling tool cannot adequately capture their geometry.

7.4 Validation of the Building Model

Overall, the horizontal and vertical validations confirm that the model is largely reliable. The footprint geometry aligns well with both the PICC data and orthophotos, and the modelled heights are, in most cases, consistent with official elevation data. However, some localised errors remain, particularly in buildings with complex or unconventional roof structures or where segmentation issues occur. These findings highlight the importance of careful post-processing when using semi-automatic tools, especially in areas with architectural complexity.

Nevertheless, several limitations exist in the validation data and methodology. For horizontal validation, both the PICC footprints and orthophotos were used; however, these datasets are not entirely independent of the modelling process. The PICC footprints served as the basis for the

3D model, and the orthophotos were used as visual references during manual adjustments, particularly for refining footprint geometry and segmentation. This interdependence may have influenced the validation results, potentially leading to an overestimation of model accuracy.

In the case of vertical validation, the eaves height from the PICC dataset was used. While this parameter can effectively validate the height of flat-roof buildings, it is insufficient for evaluating more complex roof forms, such as gabled or hipped roofs, where additional parameters like ridge height are also relevant. Thus, although eaves height provides a partial measure of vertical accuracy, it does not fully capture the model's overall vertical reliability.

Nonetheless, the overall performance of the model demonstrates that it provides a solid and accurate basis for further applications in 3D urban analysis.

7.5 Addressing the Research Questions

Based on the obtained results and the discussions presented above, this section provides answers to the two guiding research questions posed at the beginning of the study.

First, regarding the compatibility between building footprints extracted from LiDAR and those provided by PICC, the findings show that the overall similarity between the two datasets is relatively high. However, certain individual buildings exhibit lower levels of agreement. This discrepancy mainly stems from limitations inherent in the footprint extraction process using LiDAR data. Several factors contribute to these inconsistencies. First, the classification of the LiDAR point cloud may fail to detect some building areas—particularly small structures or parts obscured by vegetation—resulting in missing building elements. Second, the boundaries of the LiDAR-derived building polygons often appear jagged or irregular, lacking the smoothness of manually verified datasets. Lastly, in complex building groups, such as those where two main structures are connected by shared elements like corridors or elevator shafts, LiDAR often struggles to correctly identify and delineate each component due to small surface area and height variations in these transitional spaces.

Therefore, while LiDAR data contributes valuable 3D structural information, PICC provides more complete and validated 2D building footprints. Its official status and accuracy (±25 cm) make it a more reliable source for footprint geometry. However, since PICC does not contain any information about roof structures, LiDAR serves as an essential complementary dataset, enabling the extraction of height and roof shape.

Second, regarding the contributions of each dataset to the 3D modelling process, the results suggest that LiDAR plays a dominant role in providing geometric and elevation information. It captures accurate data about building height, shape, and general structure, making it indispensable for three-dimensional reconstruction. That said, the accuracy of the final model is somewhat reduced during the conversion of point cloud data into 3D building objects, especially in areas with complex roof geometries. Despite this, LiDAR contributes markedly to both the completeness and spatial realism of the building models, as it contains nearly all relevant 3D geometric information—though it lacks semantic data, such as building function or classification.

PICC, by contrast, offers ready-to-use, validated footprints with high positional accuracy, making it ideal for supplementing and correcting footprint data derived from LiDAR. However, it contributes less to the vertical dimension of buildings. Although the dataset includes eave height attributes, these alone are insufficient for reconstructing full 3D roof geometries, particularly without information about roof type or slope.

Finally, the orthophoto played a more limited role in this study. It was primarily used for visual inspection during manual adjustments and for validation purposes. Nevertheless, in other research contexts, orthophotos have been used for building footprint extraction or DSM generation, providing useful support for building reconstruction tasks.

7.6 Limitations

This section outlines several limitations encountered during the course of this study.

First, the primary dataset used for modelling was classified LiDAR point cloud data, which included categories such as buildings, vegetation, and ground. The extraction of building footprints relied directly on the points classified as "building." As a result, the accuracy of this classification directly influenced the quality of the final model. During the modelling process, some buildings were found to be only partially classified as "building," resulting in a sparse point cloud and, consequently, an inaccurate footprint boundary. These problematic structures were predominantly greenhouses with transparent roofs, which likely interfered with LiDAR's ability to correctly classify them. This misclassification had a noticeable impact on subsequent steps of the modelling workflow.

Second, the tool selected for building generation presented intrinsic limitations. The 3D Buildings tool, provided as part of the ArcGIS Solutions suite, was used for its ability to automate LoD2 building modelling using LiDAR data. This solution includes a sequence of tasks that guide users from point cloud to final model. While this approach markedly reduced manual workload and enabled efficient modelling through simple parameter adjustments, it also introduced certain constraints. Most of the modelling logic is embedded within the tool’s internal processes, which can only be inferred through documentation rather than directly examined or customised. This opacity may lead to conceptual ambiguities or oversights. Also, the tool has limited flexibility in some aspects—for example, roof type classification is restricted to several categories. As noted in the previous section, this constraint prevented the accurate modelling of more complex or unconventional roof structures.

Third, there were limitations in the validation strategy. Due to the lack of highly precise, independent reference models for the study area, a twofold validation method—horizontal and vertical—was employed. Datasets that were considered more reliable in each dimension were used as benchmarks. While the elevation data used in vertical validation were independent from the model, the horizontal validation involved datasets that were not fully independent. In particular, the PICC building footprints served as the foundation for the modelled footprints, albeit with subsequent manual refinements. Even though the orthophoto was only used as a reference during manual adjustment and had a looser connection to the model, it still cannot be considered fully independent. For a more careful and objective validation, an external dataset not involved in any part of the modelling process would be necessary.

Finally, a potential limitation lies in the temporal inconsistency between datasets. The LiDAR data, orthophotos, and official building footprint datasets were not acquired in the same year. Although the selected study area is relatively small and has undergone limited recent construction, temporal mismatches could still introduce minor discrepancies. This issue may become more pronounced in other urban areas with ongoing development or renovation, potentially affecting the alignment of footprints or the accuracy of elevation data. In such cases, care should be taken to account for changes in the built environment over time.

7.7 Recommendations

This study was limited to a subset of Louvain-la-Neuve. A logical next step would be to expand the analysis to cover the entire city. While this broader scope would introduce additional computational and logistical challenges, it would also increase the generalizability and applicability of the findings. At a city-wide scale, key challenges may include data processing efficiency and inconsistencies due to differences in acquisition time across datasets, especially in newly developed or under-construction areas.

In addition to spatial expansion, future work could benefit from the integration of advanced modelling techniques such as machine learning and deep learning. For instance, convolutional neural networks (CNNs) have shown promise in tasks like automatic roof type classification, footprint extraction, and 3D reconstruction(Muftah et al., 2022). These methods could overcome some limitations of semi-automated tools—such as limited roof shape types—and enable more flexible and accurate modelling across diverse building typologies.

Also, the inclusion of other complementary data sources—such as UAV imagery, temporal satellite data, or street-level photographs—may further enhance the model's completeness and realism(Gui & Qin, 2021). Incorporating such data would also allow for more dynamic and up-to-date representations of urban environments.

Finally, future research may explore developing more systematic accuracy assessment workflows, possibly integrating field validation or high-resolution ground truth data. This could help reduce the essential manual adjustments and ensure the robustness of the modelling process, especially as it scales to larger or more complex urban areas

Chapter 8. Conclusion

As urban environments become increasingly complex and urban challenges continue to emerge, employing 3D city models to simulate and monitor urban elements with greater precision is becoming ever more important. At the same time, technological advancements have led to the proliferation of diverse high-resolution datasets, each with its own advantages and limitations. Against this backdrop, this study aimed to construct a LoD2-level 3D building model for a selected urban area by using three existing high-resolution datasets. The objective was to explore the compatibility of these datasets and determine how they could be combined to maximize their respective strengths in generating the most accurate model possible.

The datasets employed included classified LiDAR point cloud data, official building footprints provided by PICC, and a high-resolution orthophoto. The modelling was carried out using the 3D Buildings tool from ArcGIS Solutions, a semi-automated framework designed for 3D urban reconstruction based on LiDAR data. The workflow first involved extracting building footprints from the LiDAR point cloud, followed by a similarity analysis between these footprints and those from the PICC dataset. The resulting LoD2-level 3D building model was then subjected to both horizontal and vertical validation.

The final model yielded promising results. A visual comparison with the original LiDAR point cloud indicated strong spatial alignment. Horizontal validation showed a high degree of consistency with both the PICC data and the orthophoto, with the observed discrepancies likely caused by segmentation differences. Vertical validation against official eave height data also confirmed the model's reliability in terms of building height accuracy. The remaining errors were mainly attributable to complex roof structures, segmentation inconsistencies, and non-standard architectural forms. Also, a similarity analysis between the LiDAR-derived and official building footprints confirmed general consistency, though the LiDAR-based outlines exhibited some unavoidable jaggedness and segmentation irregularities. Consequently, the PICC footprints were used as the base for the final 3D model.

To further assess the accuracy of the model, RMSE values were calculated based on the difference between the generated model and the LiDAR-derived DSM. Buildings with the highest RMSE values were selected for case-by-case analysis. The findings revealed that large errors were primarily due to complex roof or sub-eave structures, the presence of multiple interconnected buildings, and roof types that could not be represented by the available modelling tool.

This study contributes to the understanding of dataset compatibility regarding LoD2-level 3D building model construction. It also offers insight into how multiple datasets can be strategically integrated to improve model accuracy. The proposed methodology can work as a foundational framework for future applications such as solar potential estimation, disaster monitoring, and urban planning.

Nevertheless, several limitations remain, as discussed in Chapter 7.5. The accuracy of the LiDAR point cloud classification directly affects the precision of the derived building footprints. The 3D Buildings tool, while efficient, functions as a black-box system with limited customizability—especially in terms of roof type classification, which is restricted to a fixed set of categories and cannot accommodate more complex roof geometries. Also, the data used for model validation was not entirely independent of the modelling process: the PICC dataset formed the basis of the model, and the orthophoto, while only used for manual adjustments, still provided reference information. In addition, temporal discrepancies between datasets—although minimal in this study due to the limited area—may pose more substantial challenges in larger or rapidly changing regions.

Looking ahead, future research could focus on adopting deep learning-based approaches to improve classification flexibility and reduce reliance on semi-automated tools. Scaling the workflow to larger and more heterogeneous urban areas would also help assess its generalizability. Integrating other data sources, such as higher-resolution imagery or thermal data, may further enhance roof segmentation accuracy. Most importantly, obtaining independent and up-to-date validation datasets would be essential to verifying model reliability. Finally, applying the resulting model to practical urban analyses, such as solar potential assessment or flood risk modelling, could provide a valuable test of its real-world utility.

Reference

Abdul, H., & Sadeq, J. (2024). Generating 3D City Mesh Model Based on Aerial Imagery: A Case Study, College of Engineering Campus. *ZANCO JOURNAL OF PURE AND APPLIED SCIENCES*, *36*(2). https://doi.org/10.21271/ZJPAS.36.2.6

Adreani, L., Colombo, C., Fanfani, M., Nesi, P., Pantaleo, G., & Pisanu, R. (2022). A Photorealistic 3D City Modeling Framework for Smart City Digital Twin. *2022 IEEE International Conference on Smart Computing (SMARTCOMP)*, 299–304. https://doi.org/10.1109/SMARTCOMP55677.2022.00071

Affaire de Louvain. (2025). In *Wikipedia*. https://fr.wikipedia.org/w/index.php?title=Affaire_de_Louvain&oldid=222632784

Agugiaro, G. (2016). Energy planning tools and CityGML-based 3D virtual city models: Experiences from Trento (Italy). *Applied Geomatics*, *8*(1), 41–56. https://doi.org/10.1007/s12518-015-0163-2

Ahmed, F. C., & Sekar, S. P. (2015). Using Three-Dimensional Volumetric Analysis in Everyday Urban Planning Processes. *Applied Spatial Analysis and Policy*, *8*(4), 393–408. https://doi.org/10.1007/s12061-014-9122-2

Bahu, J.-M., Koch, A., Kremers, E., & Murshed, S. M. (2013). TOWARDS A 3D SPATIAL URBAN ENERGY MODELLING APPROACH. *ISPRS Annals of the Photogrammetry, Remote Sensing and Spatial Information Sciences*, *II-2-W1*, 33–41. WG II/2 </br> ISPRS 8th 3D GeoInfo Conference & WG II/2 Workshop (Volume II-2/W1) - 27–29 November 2013, Istanbul, Turkey. https://doi.org/10.5194/isprsannals-II-2-W1-33-2013

Biljecki, F., Stoter, J., Ledoux, H., Zlatanova, S., & Çöltekin, A. (2015). Applications of 3D City

Models: State of the Art Review. *ISPRS International Journal of Geo-Information*, *4*(4), Article 4. https://doi.org/10.3390/ijgi4042842

Boates, I., Agugiaro, G., & Nichersu, A. (2018). NETWORK MODELLING AND SEMANTIC 3D CITY MODELS: TESTING THE MATURITY OF THE UTILITY NETWORK ADE FOR CITYGML WITH A WATER NETWORK TEST CASE. *ISPRS Annals of the Photogrammetry, Remote Sensing and Spatial Information Sciences*, *IV–4*, 13–20. ISPRS TC IV Mid-term Symposium “3D Spatial Information Science – The Engine of Change” (Volume IV-4) - 1–5 October 2018, Delft, The Netherlands. https://doi.org/10.5194/isprs-annals-IV-4-13-2018

Bolte, A.-M., Niedermann, B., Kistemann, T., Haunert, J.-H., Dehbi, Y., & Kötter, T. (2024). The green window view index: Automated multi-source visibility analysis for a multi-scale assessment of green window views. *Landscape Ecology*, *39*(3), 71. https://doi.org/10.1007/s10980-024-01871-7

Buyuksalih, G., Baskaraca, P., Bayburt, S., Buyuksalih, I., & Abdul Rahman, A. (2019). 3D CITY MODELLING OF ISTANBUL BASED ON LIDAR DATA AND PANORAMIC IMAGES – ISSUES AND CHALLENGES. *The International Archives of the Photogrammetry, Remote Sensing and Spatial Information Sciences*, *XLII-4-W12*, 51–60. 5th International Conference on Geoinformation Science – GeoAdvances 2018: ISPRS Conference on Multi-dimensional & Multi-scale Spatial Data Modeling (Volume XLII-4/W12) - 10–11 October 2018, Casablanca, Morocco. https://doi.org/10.5194/isprs-archives-XLII-4-W12-51-2019

Cécile MÉCHIN. (2023). *Levé Lidar RAPPORT TECHNIQUE*. Service Public de Wallonie.

Chen, K., Lu, W., Xue, F., Tang, P., & Li, L. H. (2018). Automatic building information model reconstruction in high-density urban areas: Augmenting multi-source data with architectural knowledge. *Automation in Construction*, *93*, 22–34. https://doi.org/10.1016/j.autcon.2018.05.009

Czyńska, K., & Rubinowicz, P. (2014). *APPLICATION OF 3D VIRTUAL CITY MODELS IN URBAN ANALYSES OF TALL BUILDINGS – TODAY PRACTICE AND FUTURE CHALLENGES*.

Delikostidis I., Engel J., Retsios B., Elzakker C. P. J. M., Kraak M.-J., & Döllner J. (2013). Increasing the Usability of Pedestrian Navigation Interfaces by means of Landmark Visibility Analysis. *The Journal of Navigation*, *66*(4), 523–537. https://doi.org/10.1017/S0373463313000209

Digital Elevation Model and Digital Surface Model. (2017). *International Encyclopedia of Geography*, 1–17. https://doi.org/10.1002/9781118786352.wbieg0768

Ďuračiová, R. (2023). An Aggregated Shape Similarity Index: A Case Study of Comparing the Footprints of OpenStreetMap and INSPIRE Buildings. *ISPRS International Journal of Geo-Information*, *12*(12), Article 12. https://doi.org/10.3390/ijgi12120495

Fath, K., Stengel, J., Sprenger, W., Wilson, H. R., Schultmann, F., & Kuhn, T. E. (2015). A method for predicting the economic potential of (building-integrated) photovoltaics in urban areas based on hourly Radiance simulations. *Solar Energy*, *116*, 357–370. https://doi.org/10.1016/j.solener.2015.03.023

Fruh, C., & Zakhor, A. (2001). 3D model generation for cities using aerial photographs and ground level laser scans. *Proceedings of the 2001 IEEE Computer Society Conference on Computer Vision and Pattern Recognition. CVPR 2001*, *2*, II–II.

https://doi.org/10.1109/CVPR.2001.990921

Gröger, G., & Plümer, L. (2012). CityGML – Interoperable semantic 3D city models. *ISPRS Journal of Photogrammetry and Remote Sensing*, *71*, 12–33. https://doi.org/10.1016/j.isprsjprs.2012.04.004

Gui, S., & Qin, R. (2021). Automated LoD-2 model reconstruction from very-high-resolution satellite-derived digital surface model and orthophoto. *ISPRS Journal of Photogrammetry and Remote Sensing*, *181*, 1–19. https://doi.org/10.1016/j.isprsjprs.2021.08.025

Guth, P. L., Van Niekerk, A., Grohmann, C. H., Muller, J.-P., Hawker, L., Florinsky, I. V., Gesch, D., Reuter, H. I., Herrera-Cruz, V., Riazanoff, S., López-Vázquez, C., Carabajal, C. C., Albinet, C., & Strobl, P. (2021). Digital Elevation Models: Terminology and Definitions. *Remote Sensing*, *13*(18), Article 18. https://doi.org/10.3390/rs13183581

Hildebrandt, D., & Timm, R. (2014). An assisting, constrained 3D navigation technique for multiscale virtual 3D city models. *GeoInformatica*, *18*(3), 537–567. https://doi.org/10.1007/s10707-013-0189-8

https://www.olloweb.com A. O. : (2024, October 3). *Louvain-la-Neuve, la ville qui n'existait pas il y a 60 ans*. Voisins - Nachbarn. https://www.voisins-nachbarn.eu/fr/vn-fr/louvain-la-neuve-la-ville-qui-n-existait-pas-il-y-a-soixante-ans.html

Hwang, R.-L., Lin, T.-P., & Matzarakis, A. (2011). Seasonal effects of urban street shading on long-term outdoor thermal comfort. *Building and Environment*, *46*(4), 863–870. https://doi.org/10.1016/j.buildenv.2010.10.017

Jovanović, D., Milovanov, S., Ruskovski, I., Govedarica, M., Sladić, D., Radulović, A., & Pajić, V.

(2020). Building Virtual 3D City Model for Smart Cities Applications: A Case Study on Campus Area of the University of Novi Sad. *ISPRS International Journal of Geo-Information*, *9*(8), Article 8. https://doi.org/10.3390/ijgi9080476

Karim, H., Rahman, A. A., Azri, S., & Halim, Z. (2022). The Development of Multi-scale Data Management for CityGML-based 3D Buildings. *Geomatics & Environmental Engineering*, *16*(1), 71–94. https://doi.org/10.7494/geom.2022.16.1.71

Kemec, S., Zlatanova, S., & Duzgun, H. S. (2010). A Framework for Defining a 3D Model in Support of Risk Management. In M. Konecny, S. Zlatanova, & T. L. Bandrova (Eds.), *Geographic Information and Cartography for Risk and Crisis Management: Towards Better Solutions* (pp. 69–82). Springer. https://doi.org/10.1007/978-3-642-03442-8_5

Kolbe, T. H., & Donaubauer, A. (2021). Semantic 3D City Modeling and BIM. In W. Shi, M. F. Goodchild, M. Batty, M.-P. Kwan, & A. Zhang (Eds.), *Urban Informatics* (pp. 609–636). Springer. https://doi.org/10.1007/978-981-15-8983-6_34

Lafioune, N., & St-Jacques, M. (2020). Towards the creation of a searchable 3D smart city model. *Innovation & Management Review*, *17*(3), 285–305. https://doi.org/10.1108/INMR-03-2019-0033

Law, C., Lee, C., Lui, A. S., Yeung, M. K., & Lam, K. (2011). Advancement of three-dimensional noise mapping in Hong Kong. *Applied Acoustics*, *72*(8), 534–543. https://doi.org/10.1016/j.apacoust.2011.02.003

Lee, A., Kim, J., & Jang, I. (2020). Movable Dynamic Data Detection and Visualization for Digital Twin City. *2020 IEEE International Conference on Consumer Electronics - Asia (ICCE-Asia)*, 1–2. https://doi.org/10.1109/ICCE-Asia49877.2020.9277250

LiDAR 2021-2022 | Géoportail de la Wallonie. (n.d.). Retrieved May 25, 2025, from https://geoportail.wallonie.be/lidar

Liu, W., Lai, B., Wang, C., Bian, X., Yang, W., Xia, Y., Lin, X., Lai, S.-H., Weng, D., & Li, J. (2020). Learning to Match 2D Images and 3D LiDAR Point Clouds for Outdoor Augmented Reality. *2020 IEEE Conference on Virtual Reality and 3D User Interfaces Abstracts and Workshops (VRW)*, 654–655. https://doi.org/10.1109/VRW50115.2020.00178

Liu, W., Zang, Y., Xiong, Z., Bian, X., Wen, C., Lu, X., Wang, C., Marcato, J., Gonçalves, W. N., & Li, J. (2023). 3D building model generation from MLS point cloud and 3D mesh using multi-source data fusion. *International Journal of Applied Earth Observation and Geoinformation*, *116*, 103171. https://doi.org/10.1016/j.jag.2022.103171

Louvain-la-Neuve. (2025). In *Wikipedia*. https://fr.wikipedia.org/w/index.php?title=Louvain-la-Neuve&oldid=225045187

Lu, L., Becker, T., & Löwner, M.-O. (2017). 3D Complete Traffic Noise Analysis Based on CityGML. In A. Abdul-Rahman (Ed.), *Advances in 3D Geoinformation* (pp. 265–283). Springer International Publishing. https://doi.org/10.1007/978-3-319-25691-7_15

Maa-amet 3D. (n.d.). Retrieved December 6, 2024, from https://3d.maaamet.ee/kaart/

Muftah, H., Rowan, T. S. L., & Butler, A. P. (2022). Towards open-source LOD2 modelling using convolutional neural networks. *Modeling Earth Systems and Environment*, *8*(2), 1693–1709. https://doi.org/10.1007/s40808-021-01159-8

Özdemir, E., Remondino, F., & Golkar, A. (2021). An Efficient and General Framework for Aerial Point Cloud Classification in Urban Scenarios. *Remote Sensing*, *13*(10), Article 10. https://doi.org/10.3390/rs13101985

PICC : la référence cartographique de la Wallonie | Géoportail de la Wallonie. (n.d.). Retrieved May 25, 2025, from https://geoportail.wallonie.be/PICC

Projet Informatique de Cartographie Continue (PICC) | Géoportail de la Wallonie. (n.d.). Retrieved May 25, 2025, from https://geoportail.wallonie.be/catalogue/b795de68-726c-4bdf-a62a-a42686aa5b6f.html

Redweik, P., Catita, C., & Brito, M. (2013). Solar energy potential on roofs and facades in an urban landscape. *Solar Energy*, *97*, 332–341. https://doi.org/10.1016/j.solener.2013.08.036

S.A.M.HASHEMI. (2008). *Automatic peaks extraction from Normalized Digital Surface Model (NDSM)*.

Shiode, N. (2000). 3D urban models: Recent developments in the digital modelling of urban environments in three-dimensions. *GeoJournal*, *52*(3), 263–269. https://doi.org/10.1023/A:1014276309416

SPW ARNE & SPW Digital. (2024). *Utilisation des produits LiDAR: Focus sur les produits issus de la campagne d'acquisition aéroportée LiDAR 2021–2022* [Data description]. Service Public de Wallonie. https://geoportail.wallonie.be/files/PDF/LiDAR24/Tuto_LiDAR%202.pdf

Stoter, J., Ploeger, H., & van Oosterom, P. (2013). 3D cadastre in the Netherlands: Developments and international applicability. *Computers, Environment and Urban Systems*, *40*, 56–67. https://doi.org/10.1016/j.compenvurbsys.2012.08.008

Tarsha-Kurdi, F., Landes, T., Grussenmeyer, P., & Koehl, M. (n.d.). *Model-driven and data-driven approaches using LIDAR data: Analysis and comparison*.

Tashakkori, H., Rajabifard, A., & Kalantari, M. (2015). A new 3D indoor/outdoor spatial model for indoor emergency response facilitation. *Building and Environment*, *89*, 170–182. https://doi.org/10.1016/j.buildenv.2015.02.036

Une ville nouvelle. (n.d.). Ottignies-Louvain-la-Neuve. Retrieved May 22, 2025, from https://www.olln.be/fr/office-du-tourisme-inforville/decouvrez/les-raisons-de-venir/une-ville-nouvelle

Varduhn, V., Mundani, R.-P., & Rank, E. (2015). Multi-resolution Models: Recent Progress in Coupling 3D Geometry to Environmental Numerical Simulation. In M. Breunig, M. Al-Doori, E. Butwilowski, P. V. Kuper, J. Benner, & K. H. Haefele (Eds.), *3D Geoinformation Science: The Selected Papers of the 3D GeoInfo 2014* (pp. 55–69). Springer International Publishing. https://doi.org/10.1007/978-3-319-12181-9_4

Verdie, Y., Lafarge, F., & Alliez, P. (2015). LOD Generation for Urban Scenes. *ACM Transactions on Graphics*, *34*(3), 1–14. https://doi.org/10.1145/2732527

Verma, V., Kumar, R., & Hsu, S. (2006). 3D Building Detection and Modeling from Aerial LIDAR Data. *2006 IEEE Computer Society Conference on Computer Vision and Pattern Recognition (CVPR'06)*, *2*, 2213–2220. https://doi.org/10.1109/CVPR.2006.12

virtualcitySYSTEMS. (2017, January 1). *virtualcityMAP - 3D-Stadtmodelle im Browser*. virtualcitySYSTEMS. https://www.virtualcitysystems.de

VISITWallonia. (n.d.). *Ottignies—Louvain-La-Neuve*. Retrieved May 22, 2025, from https://visitwallonia.com/en-gb/3/where-to-go/walloon-towns-and-cities/ottignies-louvain-la-neuve?cookie_lang=en-gb

Wang, F., Zhou, G., Hu, H., Wang, Y., Fu, B., Li, S., & Xie, J. (2023). Reconstruction of LoD-2

Building Models Guided by Façade Structures from Oblique Photogrammetric Point Cloud. *Remote Sensing*, *15*(2), Article 2. https://doi.org/10.3390/rs15020400

Wang, Y., Huang, X., & Gao, M. (2022). 3D MODEL OF BUILDING BASED ON MULTI-SOURCE DATA FUSION. *The International Archives of the Photogrammetry, Remote Sensing and Spatial Information Sciences*, *XLVIII-3-W2-2022*, 73–78. ISPRS TC III & TC IV
Urban Geoinformatics 2022 - 1–4 November 2022, Beijing, China. https://doi.org/10.5194/isprs-archives-XLVIII-3-W2-2022-73-2022

Wen, C., You, C., Wu, H., Wang, C., Fan, X., & Li, J. (2019). Recovery of urban 3D road boundary via multi-source data. *ISPRS Journal of Photogrammetry and Remote Sensing*, *156*, 184–201. https://doi.org/10.1016/j.isprsjprs.2019.08.010

Xie, F., Lin, Z., Gui, D., & Lin, H. (2012). STUDY ON CONSTRUCTION OF 3D BUILDING BASED ON UAV IMAGES. *The International Archives of the Photogrammetry, Remote Sensing and Spatial Information Sciences*, *XXXIX-B1*, 469–473. XXII ISPRS Congress, Technical Commission I (Volume XXXIX-B1) - 25 August – 01 September 2012, Melbourne, Australia. https://doi.org/10.5194/isprsarchives-XXXIX-B1-469-2012

Yan, J., Zlatanova, S., Aleksandrov, M., Diakite, A. A., & Pettit, C. (2019). INTEGRATION OF 3D OBJECTS AND TERRAIN FOR 3D MODELLING SUPPORTING THE DIGITAL TWIN. *ISPRS Annals of the Photogrammetry, Remote Sensing and Spatial Information Sciences*, *IV-4-W8*, 147–154. ISPRS WG IV/10
14th 3D GeoInfo Conference 2019 (Volume IV-4/8) - 24–27 September 2019, Singapore. https://doi.org/10.5194/isprs-annals-IV-4-W8-147-2019

Ying, Y., Koeva, M., Kuffer, M., & Zevenbergen, J. (2023). Toward 3D Property Valuation—A

Review of Urban 3D Modelling Methods for Digital Twin Creation. *ISPRS International Journal of Geo-Information*, *12*(1), Article 1. https://doi.org/10.3390/ijgi12010002

Zhu, Q., Hu, M., Zhang, Y., & Du, Z. (2009). Research and practice in three-dimensional city modeling. *Geo-Spatial Information Science*, *12*(1), 18–24. https://doi.org/10.1007/s11806-009-0195-z

Appendix

9.1 LiDAR derived DTM (a), DSM (b), nDSM (c)

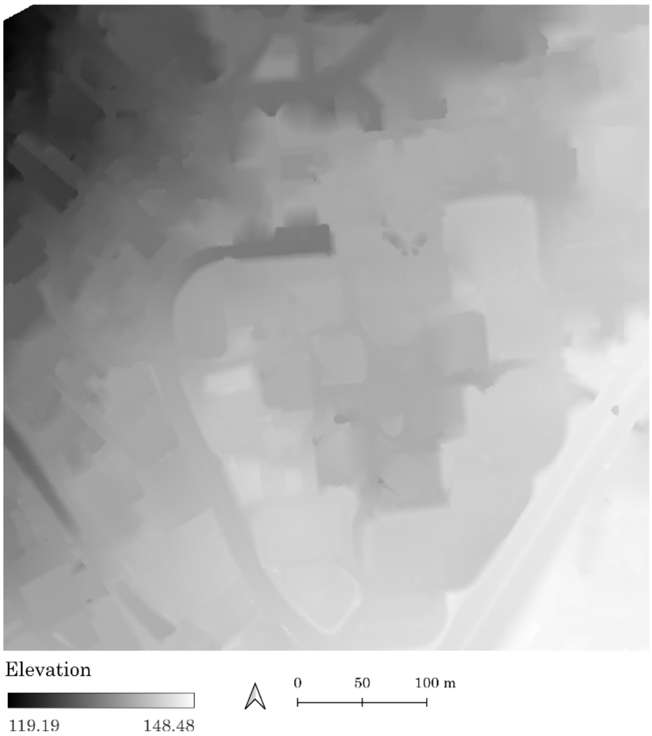

(a)

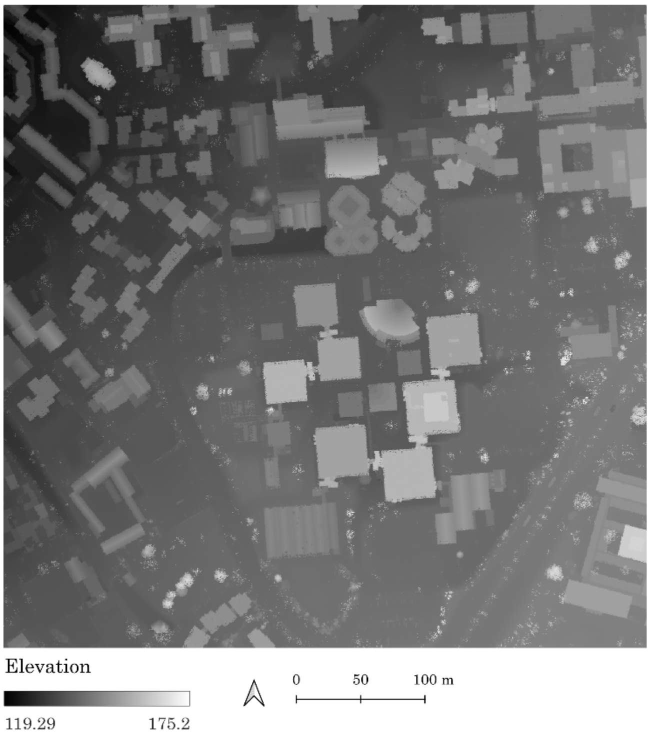

(b)

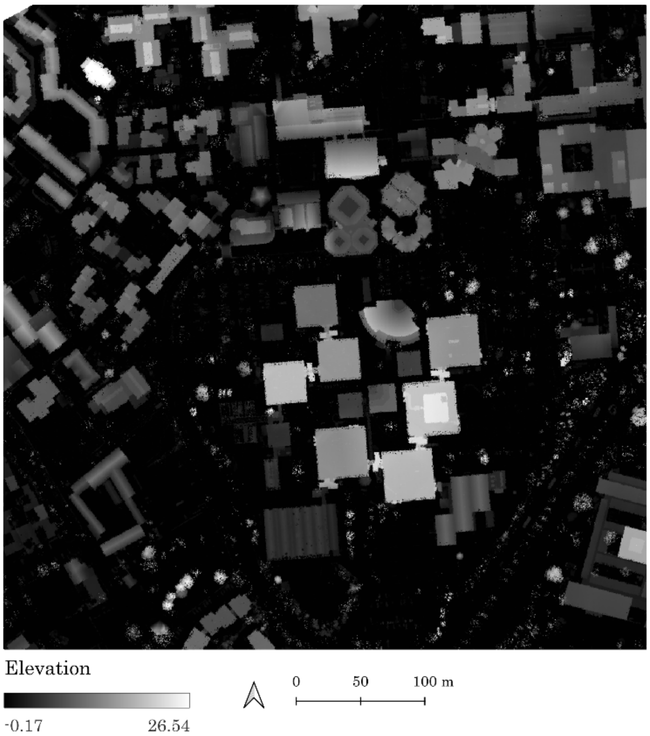

(c)

9.2 Raster building footprint derived from LiDAR point cloud using different sampling values (left: 0.3m; right: 0.5m)

9.3The final cleaned and regularized building footprint from Lidar point cloud

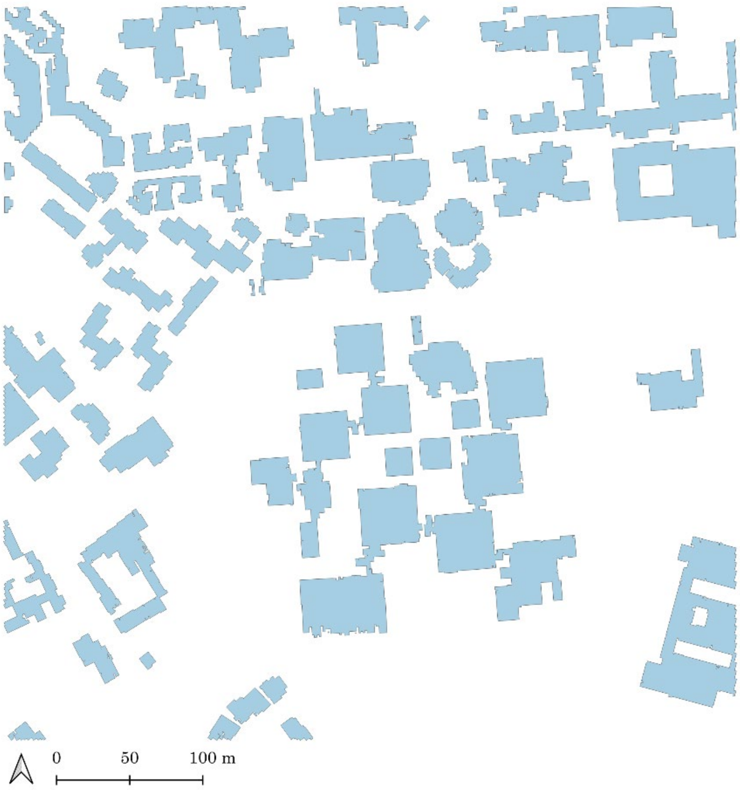

9.4 Python script used for RMSE calculation

```
import arcpy
import numpy as np
from arcpy.sa import ExtractByMask
arcpy.CheckOutExtension("Spatial")

def calc_model_height(base, height, eave, roof_type):
    roof_type = roof_type.lower()
    if roof_type == "flat":
        return base + height
    elif roof_type == "gable" or roof_type == "shed":
        #Use the average of eave and ridge
        if eave is not None:
            return base + (eave + height) / 2
        else:
            return base + height * 0.9    # fallback
    elif roof_type == "hip":
        return base + height * 0.85
    elif roof_type == "dome":
        return base + height * 0.7
    else:
        return base + height

def compute_rmse(dsm_raster, building_shape, model_height):
    try:
        clipped = ExtractByMask(dsm_raster, building_shape)
        arr = arcpy.RasterToNumPyArray(clipped, nodata_to_value=np.nan)
        valid = arr[~np.isnan(arr)]
        if len(valid) == 0:
            return None
```

```
            errors = valid - model_height
            rmse = np.sqrt(np.mean(errors ** 2))
            return rmse
        except Exception as e:
            print(f"Error computing RMSE: {e}")
            return None

building_layer = "footprint_10_roofform_roofform"
dsm_raster = "dsm_repro"
output_field = "RMSE_2"

if output_field not in [f.name for f in arcpy.ListFields(building_layer)]:
    arcpy.AddField_management(building_layer, output_field, "DOUBLE")

with arcpy.da.UpdateCursor(building_layer, ["SHAPE@", "BASEELEV", "BLDGHEIGHT",
"EAVEHEIGHT", "ROOFFORM", output_field]) as cursor:
    for row in cursor:
        shape, base, height, eave, roof, _ = row
        model_h = calc_model_height(base, height, eave, roof)
        rmse_val = compute_rmse(dsm_raster, shape, model_h)
        if rmse_val is not None:
            row[5] = rmse_val
            cursor.updateRow(row)
        else:
            print(f"Skipped building with roof '{roof}' due to no valid DSM pixels.")

print("Finished RMSE calculation.")
```

Integrating Existing High Resolution Geospatial Datasets for LoD2 Building Modelling : Accuracy Evaluation and Comparative Analysis in Louvain-la-Neuve

Kailu Chen

Accurate representation of the built environment is essential for urban planning, analysis, and decision-making. This thesis focuses on constructing a detailed 3D building model of Louvain-la-Neuve by integrating multiple high-resolution spatial datasets. Specifically, the study assesses the compatibility between LiDAR and PICC building footprints, and examines how each dataset contributes to the generation of Level of Detail 2 (LoD2) building models.

To achieve this, building footprints from both datasets were compared in terms of geometric alignment, shape similarity, and attribute completeness. The study also evaluated how differences in data resolution and classification quality influence the modeling process. A semi-automated 3D building modeling workflow was implemented using rule-based methods, and the resulting model was assessed for geometric accuracy against a LiDAR-derived digital surface model (DSM).

The findings reveal notable differences in footprint precision and roof segmentation accuracy between the datasets. While LiDAR provides more detailed elevation data, PICC offers consistent and cartographically clean building outlines. Their integration improves the overall completeness of the model but introduces challenges in data fusion and height assignment.

This research highlights the importance of understanding dataset interoperability when generating LoD2 building models and offers practical insights into the contributions and limitations of different data sources. The results aim to support future applications in urban analysis and sustainable city planning for Louvain-la-Neuve.

UNIVERSITÉ CATHOLIQUE DE LOUVAIN
Faculté des bioingénieurs
Croix du Sud, 2 bte L7.05.01, 1348 Louvain-la-Neuve, Belgique | **www.uclouvain.be/agro**